Highly nanocrystalline Mg doped $ZnFe_2O_4$ powders for rapid and simultaneous adsorption of Lead, Copper, and Cadmium heavy metals ions in synthetic / sea waters

Basma Al-Najar[a], Abueliz Modwi[b], M. Nasiruzzaman Shaikh[c], Mohamed Bououdina[d], Hanan Albuflasa[a] Nicholas P. Hankins[e]

[a] Department of Physics, College of Science, University of Bahrain, P.O. Box 32038, Sakhir Campus, Bahrain

b Department of Chemistry, College of Science and Arts, Department of Chemistry, College of Science and Arts, Qassim University, Riyadh Saudi Arabia

[c] Interdisciplinary Research Center for Hydrogen and Energy Storage (IRC-HES), King Fahd University of Petroleum and Minerals (KFUPM), Dhahran, Saudi Arabia

[d] Department of Mathematics and Sciences, Faculty of Humanities and Sciences, Prince Sultan University, Riyadh, Saudi Arabia

[e] Department of Engineering Science, The University of Oxford, Parks Road, OX3 1PJ, Oxford, UK

Abstract

This research aims to investigate the effect of Mg doping on individual and simultaneous adsorption of Pb^{+2}, Cu^{+2}, and Cd^{+2} heavy metals in aqueous solution and in seawater samples, by Zinc ferrite nanoparticles. The Mg-doped Zinc ferrite nanoparticles are synthesized successfully by the sol-gel route and varying Mg concentrations. TEM, XRD, FTIR, Raman, and XPS characterizations confirm the cubic spinel structure of Zinc ferrite with a semi-spherical shaped nanosized particles (10-15 nm) irrespective of Mg doping content. The BET surface area manifests a significant increase within Mg doping (39.3 m^2/g) compared with the pure zinc ferrite (28.4 m^2/g). Accordingly, Mg-doped Zinc ferrite powders demonstrate considerable adsorption capacities for Pb^{+2} (143.5 mg/g), Cu^{+2} (117 mg/g), and Cd^{+2} (77 mg/g) within 2 h under optimized experimental conditions. The prepared nanopowders exhibit high selectivity towards Pb^{+2} in simultaneous adsorption in aqueous solutions (85 mg/g) and real seawater samples. Nonetheless, the selectivity of Pb^{+2} ions drops dramatically to 25 mg/g within real seawater samples due to the strong ionic strength of high-salinity seawater. This study provides insights into the importance of doped spinel ferrite nanoparticles in highly efficient, rapid, and simultaneous adsorption of heavy metals. Besides, it reveals the challenge of performing the adsorption process in real seawater.

Keywords: Mg-doped Zinc Ferrite; Simultaneous adsorption; Heavy Metals; BET surface area; XPS; seawater.

1. Introduction

The tremendous pollution of water basins has been one of the most serious environmental issues that is threatening human being and species habitats (Zhang et al., 2022; Zhao et al., 2019). Most of the pollutants diffuse to the aquatic systems because of industrial activities. This includes organic and inorganic traces that are found in lakes, rivers and even seawater (Abdulla & Naser, 2021). Inorganic pollutants are mainly ions of heavy metals that are discharged from industrial firms (Soultanidis et al., 2022). Heavy metals ions of Lead (Pb^{+2}), Cadmium (Cd^{+2}), Copper (Cu^{+2}), Arsenic (As^{+4}) and Chromium (Cr^{+3}) are discovered in rivers (Çelebi et al., 2020; Paul, 2017), lakes (Nasiri et al., 2018), and seawater (Bersuder et al., 2020; Yang et al., 2019) and are reported to cause serious toxicity issues to human health and environment (Kinuthia et al., 2020; Miranda et al., 2022; Obasi & Akudinobi, 2020; Thomas & Alexander, 2020; Yang et al., 2019).

The search of a cost-effective process for removing heavy metals has been a continuous challenge for decades. Nanoparticles emerge as one of the most efficient adsorbents for heavy metals removal within aqueous solutions (Chauhan et al., 2022; Darling, 2018; Rastgar et al., 2017; Tatarchuk et al., 2020). In general, the extremely small unit size of nanoparticles owe them fascinating structural and surface properties that lead to a remarkable behavior within surroundings (Fayazzadeh et al., 2020; Mmelesi et al., 2021). Compared with their bulk counterparts, their enhanced optical and magnetic properties make them highly responsive materials with potential applications including energy harvesting (Liu et al., 2020), photocatalysis (Ong et al., 2018), and adsorption process (Asadi et al., 2020; Xiang et al., 2020). In particular, ferrites nanoparticles were introduced lately as one of the most cost-efficient oxides family due to the unique cubic structure that can be tuned through several approaches resulting enhanced properties thereby directly affecting their performance. Ferrite nanoparticles own chemical formula of MFe_2O_4 (M =, Co, Ni, Mn, Mg, Cu and Zn, etc) and crystallize within a simple cubic structure where the atoms are distributed within octahedral and tetrahedral lattice sites (Ashok et al., 2020)(Somvanshi et al., 2020). It is very interesting to mention that there are of 97 A and B sites, that can be occupied by only 24 cations, in different configurations (Aisida et al., 2020; Al Maashani et al., 2020; Bhushan Das et al., 2021). The exchange of atoms within tetrahedral and octahedral sites within the ferrite lattice is one of the most unique structures

that can cause major properties' alteration at the nanoscale. The change in size, shape, and structural defects of metal ferrite nanoparticles manifests noticeable influence in water treatment applications (Nimshi et al., 2023)(Reddy & Yun, 2016). Researchers aim to manipulate the ferrite structure primarily by investigating different synthesis approaches to change shape, size and/or create structural defects such oxygen/metal vacancies. Considering structural defects, self-doping (F. Wang et al., 2017; Wu et al., 2018, 2019) and different metal doping (Hareendran et al., 2022; Punia et al., 2022; Vinosha et al., 2022a) represent the two main approaches that been applied to enhance the surface structure, size, porosity, as well as optical and magnetic properties. Therefore, doped ferrites have been applied lately in water treatment applications, in particular, photocatalysis of inorganic pollutants (Long et al., 2022; Shakil et al., 2022) and in adsorption of heavy metals (A. Ivanets, Prozorovich, Kouznetsova, et al., 2021a; Tatarchuk, Myslin, et al., 2021; Tatarchuk, Shyichuk, et al., 2021). If we consider the adsorption of heavy metals using ferrites nanoparticles, there are several considerations and concerns that can be summarised in the following points.

First, the structure of the doped ferrite adsorbents applied for heavy metals ions. Recent studies revealed the effect of doping the ferrite structure on its ability to adsorb different types of heavy metals (Mary et al., 2023). Defective magnesium ferrite showed enhanced adsorption ability toward As^{+4} as a result of increased surface hydroxyl groups (Wu et al., 2018). Also, magnesium-zinc ferrites were applied efficiently to remove Cr^{+3} and Ni^{+2} ions from aqueous solutions (Tatarchuk, Myslin, et al., 2021). The Zn and Ni co-doped $MgFe_2O_4$ (20-100%) ferrite system demonstrated that the maximum adsorption of Cr^{+3} has been achieved at Zn content of 80% while for Ni^{+2} only 60% Zn doping, after 24 h of reaction time. The change in the efficiency of reaction along with doping was correlated with the active sites present at the surface of ferrite nanoparticles which are in turn were influenced by the amount of doping. Cobalt doped Zinc ferrites nanoparticles were also applied for the removal of Pb^{+2} (Tatarchuk, Myslin, et al., 2021). The study applied different ferrite compositions representing the conversion from pure Zinc ferrite structure to Cobalt ferrite structure starting with 20% of weight doping percentage. The pure zinc ferrite showed a maximum adsorption capacity of 30.49 mg/g toward Pb^{+2} ions, which was related to the strength of interatomic bonds in pure zinc ferrites, while doping with larger

atoms of Co would decrease the ionic covalent parameter. To the best knowledge of authors, no previous studies in the literature have investigated the effect of small amount of doping (less than 10%) on the adsorption capacity of zinc ferrite nanoparticles, though such small amount of doping could alter the ferrite nanoparticles' morphology and surface properties (Jyothish & Jacob, 2021; Vinosha et al., 2022b). Applying small doping to a certain ferrite structure may enhance their physicochemical properties without interfering with its major lattice structure and interatomic characteristics. Therefore, it is worthwhile to scrutinise the effect of small metal ion defects on the adsorption of heavy metals from aqueous solutions. In this work, Mg was chosen as doping element due to its smaller ionic radius, compared to Zn, that may lead to smaller pores and hence high surface area. Also, Mg forms an inverse spinel which will cause rearrangement of ions within the tetrahedral and octahedral sites in the normal spinel structure of $ZnFe_2O_4$. This will be accompanied by changes in the surface functional groups on the ferrite structure, and thereby, enhance its adsorption ability towards heavy metal ions.

Second, the efficiency of the reaction is very important to assess the performance of the whole process as well as the adsorption capacity and the time of the reaction. Most of the studies reported in the literature that investigated doped ferrite systems have shown low adsorption capacity, in comparison with other nanoadsorbents, besides a longer contact time ranging from 2 to 24 h.

Third, it is very essential to mention that the adsorption reaction depends strongly on the operational conditions including pH, temperature, ionic strength of the solution, and the existence of other heavy metal ions and pollutants. The competitive/multiple ions adsorption is a critical indicator of the effectiveness of the adsorbent and its applicability in real life applications. Researchers are also investigating the adsorption process within real water samples to have more realistic results about the adsorption performance. A recent study showed a great performance of pure magnesium ferrite in the competitive adsorption of Cu^{+2}, Co^{+2}, Ni^{+2} and Mn^{+2} (Ivanets et al., 2021). According to our literature survey, other pure and doped ferrite structures were not intensively investigated yet in the multiple adsorptions of heavy metal as well as in real water samples.

This research work aims to investigate the effect of small percentage of Mg doping (less than 10%) on the crystal structure stability, particles' morphology and size distribution, and surface properties on individual and simultaneous adsorption of Pb^{+2}, Cd^{+2}, and Cu^{+2} heavy metals ions in aqueous solution and seawater samples. Particular emphasis is devoted to examining primarily the effects of concentration, pH, and reaction time, as well as modelling of the adsorption process and kinetics using conventional isotherms. This article gives an insight of the importance of very small defects within the ferrite crystal structure that can markedly enhance its adsorption ability due to remarkable changes on its properties.

2. Methodology

2.1 Synthesis of Mg doped zinc ferrite nanoparticles

Samples of Mg doped $ZnFe_2O_4$ (ZFN) nanoparticles doped with different amounts of Mg were synthesized by sol-gel method. Equal amounts of citric acid and $Fe(NO_3)_3{\cdot}9H_2O$ were added to distilled water along with specific amounts $Zn(NO_3)_2$ and $Mg(NO_3)_2$. The schematic ratios of precursors molar mass were calculated as per (Rashdan & Hazeem, 2020) previous work. The percentage weight ratio of $Zn(NO_3)_2$ and $Mg(NO_3)_2$ was applied as follows, 100:0 wt%, 97.5:2.5 wt%, 95:5 wt%, 92.5:7.5 wt% and 90:10 wt%. After 25 min of magnetic stirring, Ammonium Hydroxide was added to the solution to adjust the pH to 7. Then, the solution was heated to 130°C along with continuous stirring until it is completely evaporated and burned into black powder. The fabricated samples were denoted as ZFN, ZFN-Mg-1, ZFN-Mg-2, ZFN-Mg-3 and ZFN-Mg-4, for the pure $ZnFe_2O_4$, $Mg_{0.025}Zn_{0.975}Fe_2O_4$, $Mg_{0.05}Zn_{0.95}Fe_2O_4$, $Mg_{0.075}Zn_{0.925}Fe_2O_4$ and $Mg_{0.1}Zn_{0.9}Fe_2O_4$, respectively.

2.2 Characterization of Mg doped zinc ferrite nanoparticles.

The morphology of ZFN-Mg particles was investigated by transmission electron microscopy (TEM Talos L120C G2- LaB6). The crystallite structure and phase composition were determined by X-ray diffraction (XRD) using Rigaku Ultima IV equipped with Cu-Kα radiation source (0.15418 nm) with angle ranging from 10º to 80º. Fourier- transformation infrared spectroscopy (FTIR) measurements were performed using Shimadzu- IRAffinity-1S apparatus to examine the bonding and surface functional groups.

The optical properties were investigated using UV–vis spectroscopy (Shimadzu-Lambda-4B). Raman Spectroscopy and X-ray Photoelectron Spectroscopy (XPS) were also used to investigate the absorption, binding states, and the elemental composition of the samples. The N_2 adsorption-desorption isotherm measurements were performed using a Micromeritics Chemi Sorb 2750. The Brunauer–Emmett–Teller (BET) method, with a degassing temperature of 300°C for 180 min, was applied to determine the surface area and pore structure. The pore-size distribution (PSD) was obtained from the adsorption branch of the isotherms through the Barrett–Joyner–Halenda (BJH) method.

2.3. Adsorption of Pb^{+2} ions onto Mg doped zinc ferrite nanoparticles

All samples were investigated for the adsorption of Pb^{+2} ions in aqueous solution. The best sample were selected for further experiments. Batch study of Pb^{+2} ions adsorption was conducted by applying 10 mg of ZFN samples (ZFN-500, ZFN-Mg-1, ZFN-Mg-2, ZFN-Mg-3 and ZFN-Mg-4) in 25 mL distilled water with Pb^{+2} ion concentration of 60 mg/L. Pb ion solutions were obtained from (Stock Solution-Sigma Aldrich– 1000 mg/L) and diluted subsequentially until it reached 60 mg/L. Pb^{+2} ions and ZFN samples were placed in orbital shaker at orbital speed of 130 rpm under 25°C for 1 h. To determine the adsorption efficacy, the solution was filtered to remove the subjected ZFN adsorbent. Then, the concentration of Pb^{+2} ions was measured using Inductive Coupled Plasma (ICP) analysis and compared with the control sample (No ZFN applied). The adsorption capacity was calculated using the equation below:

$$q_e = \frac{(C_0 - C_e) \times m}{V} \qquad (1)$$

Also, the removal efficiency (R%) is calculated using the equation:

$$(R\%) = \frac{(C_0 - C_e)}{C_0} \times 100 \qquad (2)$$

where q_e is the equilibrium adsorption capacity, C_0 is the initial concentration of heavy metal ions, C_e is the equilibrium concentration, *V* is the solution volume and *m* is the mass of ZFN adsorbents.

The ZFN sample with the highest adsorption capacity was chosen for further experiments. These experiments include adsorption kinetics, the effect of concentration, the effect of pH, recyclability, the ability to adsorb other heavy metal ions and simultaneous adsorption in seawater. Details of conducting these experiments are discussed below.

2.4 Zero-point charge experiment

It is well-known that the surface charge of the adsorbent contributes to its adsorption properties within the aqueous solution. The zero-point charge was measured by pH drift method. Several solution samples (10 mL) were prepared with initial pH values set to 2, 3, 4, 5, 6, 7, 8, 9, 10 using 0.1 M NaOH and 0.1 M HCl solution, these pH values are noted as pH initial. ZFN-Mg-3 was added to the prepared solutions and then, the pH was measured after 2 hrs and noted as pH final. The pH point zero charge is the point where $pH_{initial} = pH_{final}$ representing the difference between the initial and final pH (ΔpH), is zero. The pH zero charge is used as an indicator of the abundancy of surface charges of the adsorbent in solutions. Depending on the value of ΔpH, the surface charge increases positively or negatively.

2.5 Effect of initial concentration and pH

To investigate the effect of concentration and to calculate the adsorption isotherms, the concentration of the heavy metal ions was varied (5, 15, 30, 45, 60, 100, 200 mg/L). The same experimental setup of the adsorption kinetics batch experiment was adopted. Applying the same experimental setup, the pH was varied at 1, 3, 5, 7 and 8, using NaOH and HCL (0.1M) solutions. Moreover, the zero-point charge was measured by pH drift method.

2.6 Recyclability and stability of Mg doped zinc ferrite nanoparticles

The recyclability was investigated by applying ZFN-Mg-3 sample for another batch experiment over four cycles. After each adsorption experiment, the sample was removed from the solution by filtered paper, dried for 24 h (50°C) and used again in another adsorption experiment. The stability of the sample was investigated too by conducting XRD, FTIR, and TEM for the selected sample subjected to filtration and drying after adsorption experiment.

2.7 Single and simultaneous adsorption of Pb^{+2}, Cd^{+2} and Cu^{+2} ions in distilled water and seawater

The selected ZFN sample was also investigated in batch experiments for the adsorption of Cd^{+2} and Cu^{+2} ions. Separate experiments of kinetics, isotherms, pH effect, and recyclability were conducted for each heavy metal ions using the same operating conditions and procedure of Pb^{+2} ions experiment. The adsorption batch experiment was applied to (Pb^{+2}, Cd^{+2}, Cu^{+2}) ions simultaneously using ZFN-Mg-3. Stock solutions of Pb (1000 mg/L), Cd (1000 mg/L) and Cu (1000 mg/L) were subjected to substantial dilution until reaching the required concentration. The experiment was performed under the similar conditions of 25 mL solution size and 10 mg of ZFN. The concentration of each heavy metal ion was 60 mg/L and the pH was fixed to 7. The samples were subjected to 2 h of orbital shaking at 130 rpm and 25 °C.

Furthermore, the same experiment was performed using seawater samples from different locations in The Kingdom of Bahrain shores. The same concentrations and operating parameters were applied, but the pH was kept the same (pH = 8, conductivity = 65.47 mS/cm). Prior experiment, all collected seawater samples were tested for heavy metal contaminants using ICP, and the analysis confirmed the absence of heavy metals traces in the samples.

3. Results and Discussion

3.1. Morphology and structure of ZFN adsorbents

The high-resolution transmission electron microscopy (HRTEM) images of the prepared pure and Mg doped $ZnFe_2O_4$ nanoparticles (ZFN, ZFN-Mg-1, ZFN-Mg-2, ZFN-Mg-3, and ZFN-Mg-4) are shown in Figure 1(a to d) with 50 nm scale bar. The images' insets reveal a more focused view of 10 nm scale bar for better imaging of grain size. The images reveal a homogenous distribution of the particle size for all samples, which can be clearly viewed in the larger scale. A semi-spherical shape can be noticed for all samples. The size of the prepared ZFN samples is not really affected by Mg doping, as all images reveal almost the same grain size within a narrow range from 10 to 15 nm, as estimated by the high-resolution views. Also, the crystal lattice fringes of all prepared ZFN samples remain the same with d-spacing of 0.25 nm corresponding to the (311) plane of the crystalline cubic structure of

zinc ferrite phase, as shown in the images' insets. Such a small amount of Mg doping (less than 10 % w/w%) used in this work has not manifest any major effect on the grain morphology/size and the crystal d-spacing of the zinc ferrite. Most of the reviewed literature studies have confirmed the unnoticeable effect of small amount of metal doping on the grain morphology/size and crystal lattice of ferrite nanostructure (Ashok et al., 2021; Vinosha et al., 2022a). Figure 1f shows a highly magnified image of ZFN-Mg-3 sample revealing a clear crystal plane of a typical cubic structure. The inset in Figure 1 f shows the selected area electron diffraction (SAED) pattern of the sample, whereas the face centred cubic (FCC) crystal structure (Fd–3m space group) of the zinc ferrite structure is confirmed.

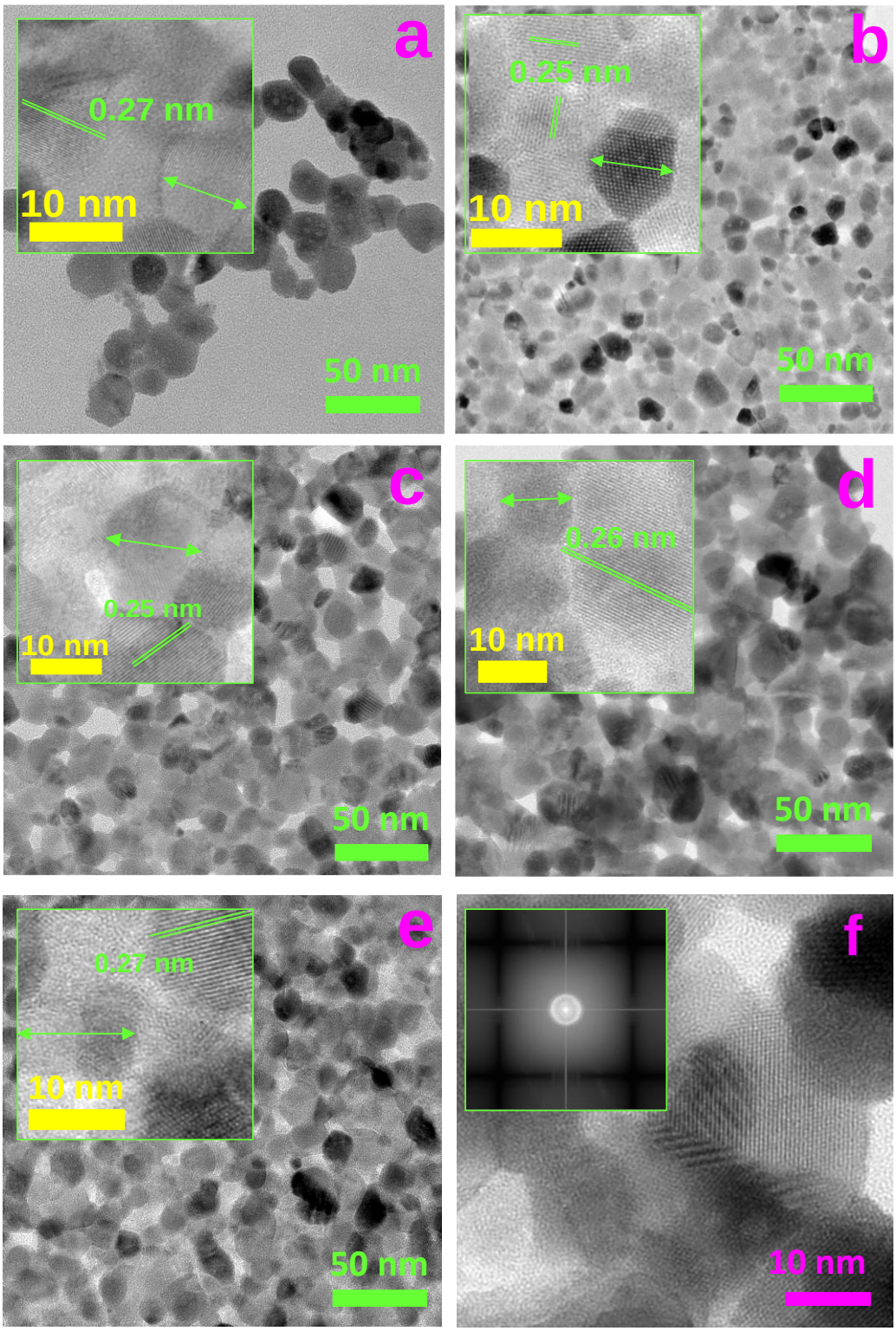

Figure 1. HRTEM images of (a)ZFN, (b)ZFN-Mg-1, (c) ZFN-Mg-2, (d) ZFN-Mg-3, (e) ZFN-Mg-4, (f) higher magnification ZFN-Mg-3 (Inset: SAED pattern).

3.2. Crystal structure of Mg doped ZFN adsorbents

The X-ray diffraction (XRD) patterns of the prepared pure and Mg doped $ZnFe_2O_4$ are shown in Figure 2 a. Well-defined diffraction peaks appear in all samples corresponding to the typical structure of a normal spinel phase. The peaks located at $2\theta = 18.2°$, 29.9°, 35.2°, 36.8°, 42.8°, 53.1°, 56.7°, 62.2° and 73.6° correspond to the crystal planes (111), (220), (311), (222), (400), (422), (511), (440) and (533), respectively, in the pattern of zinc ferrite lattice confirming the formation of the spinel crystalline phase. No additional peaks are detected within the XRD patterns, indicating the high purity of the prepared pure and Mg doped $ZnFe_2O_4$. The crystal parameters for the prepared samples obtained by the Rietveld analysis are given in Table S1, in supporting document alongside the refined XRD patterns (Figure S1, where the blue pattern is the calculated and the red pattern is the observed pattern, whereas the pink line represents the difference). All observed XRD patterns are found to fit very well with the calculated patterns of the software library JCPDS No. 01-078-6543 with a space group of Fd-3m. The fitting parameters (i.e. the factors of the Rietveld analysis) (Toby, 2006) are given in Table S1 along with calculated crystallite size, microstrain, and lattice parameter. The crystallite size is found to be almost constant irrespective the amount of Mg doping, the values are set in a narrow range from 10 to 12 nm. Indeed, this is an excellent agreement with the grain size observed in TEM images, indicating that the adopted synthesis route under the optimized experimental conditions favour the growth of nanocrystals. Similarly, it is noted that the lattice parameter of the cubic phase remains constant, i.e., ~ 8.440 Å for all prepared samples.

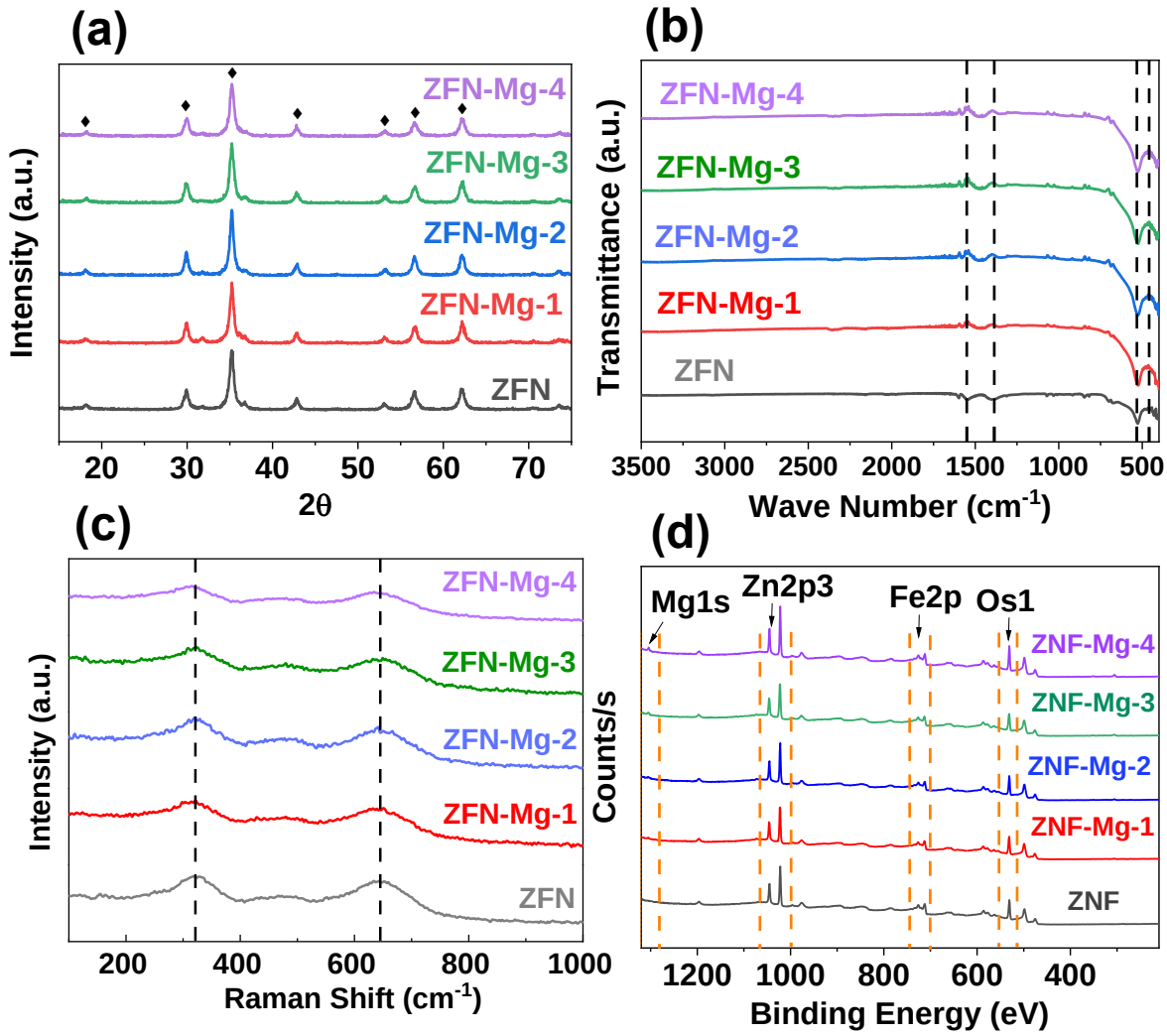

Figure 2. (a) XRD, (b) FTIR, (c) Raman and (d) XPS satellite view for Mg doped zinc ferrite nanoparticles.

3.3. Band and Energy structure

To investigate the chemical functional groups of the ferrite structure, all prepared samples have been subjected to attenuated total reflectance-Fourier transform infrared spectroscopy (ATR-FTIR), as shown in Figure 2 b. All recorded spectra display similarities in peaks' position and intensity indicating stable structure even upon Mg doping. Upon the small amount of doping, no major changes are expected in ATR-FTIR spectrum of the spinel phase $ZnFe_2O_4$, as reported in previous studies (Slatineanu et al., 2011). The two first characteristics peaks located at 430 cm^{-1} and 570 cm^{-1} are the most commonly observed

in spinel ferrite structure as they are related to the intrinsic vibrations in the A-sites (tetrahedral) and B-sites (Octahedral) within the cubic lattice structure (Khizar et al., 2020; Zakiyah et al., 2015). The third peak around 1500 cm^{-1} can be assigned to the stretching and bending vibrations of H-O-H bands, representing water molecules bonding (Shah et al., 2021; Vinosha et al., 2017).

Raman spectroscopy analysis has been also conducted to obtain further insight into the structure of the prepared zinc ferrite nanoparticles doped with different amounts of Mg. As shown in Figure 2 c, three main Raman bands are noticeably observed in the range between 200 and 1000 cm^{-1}. According to previous reports, these bands are typically found in ferrite structure, known as the three first order Raman modes, that exist specifically at 300, 500, 700 cm^{-1}. These modes correspond to the F2g(2), F2g(3) and A1g F2g(2), F2g(3) and A1g symmetries within the zinc ferrite with a cubic structure (Derakhshani et al., 2021; Rivero et al., 2016). By comparing the Raman spectra for pure ZFN and Mg doped samples, in term of peaks' position and intensity, a slight decrease in peaks' intensity can be noticed as Mg doping amount increases from 2.5 % to 10 %. Also, a very slight fluctuation is noticed for the position of the peak located around 300 cm^{-1}, which can be associated with the doping effect, since Mg ions will be incorporated within the ferrite cubic structure of $ZnFe_2O_4$ and occupy Zn ions sites (Jasrotia et al., 2020; Thota et al., 2016).

To further confirm the chemical composition of the synthesised pure and Mg doped zinc ferrite samples and to validate the existence of Mg ions within their valency state, XPS measurements have been performed. As shown in Figure 2 d, the survey XPS spectra reveal the presence of Zn, Fe and O elements, thereby confirming the chemical composition of the prepared zinc ferrites. The characteristic peaks of the zinc ferrite structure are identified clearly in all samples as Zn2p3/2, Fe2p and O1s. Moreover, a small peak of Mg1s appears in the Mg doped sample ZFN-1 and grow gradually as the doping amount increases, hence confirming the Mg existence within the parent zinc ferrite structure (Reddy & Yun, 2016; Shanmugavani & Selvan, 2014). The high-resolution spectra for individual peaks are shown in Figure 3. In Figure 3 a, the position and intensity of O1s peak shows slight fluctuation as Mg doping increases from 2.5 to 10 %, while Fe2p and Zn2p3/2 peaks become slightly sharper as shown in Figure 3 (b and c). Such fluctuation in O1 s peak may be attributed to the change in the surface functional groups that is caused

by doping. As the Mg content increase, the Mg1s peak increases noticeable, as shown in Figure 3 d, confirming the gradual incorporation of Mg ions within the ferrite structure. The above noticeable changes in XPS spectra can be attributed to the movement of O_2 atoms between the A- sites and B-sites within the ferrite lattice structure caused by Mg doping as shown Figure 3 d. Previous work have reported similar phenomena (Heiba et al., 2020).

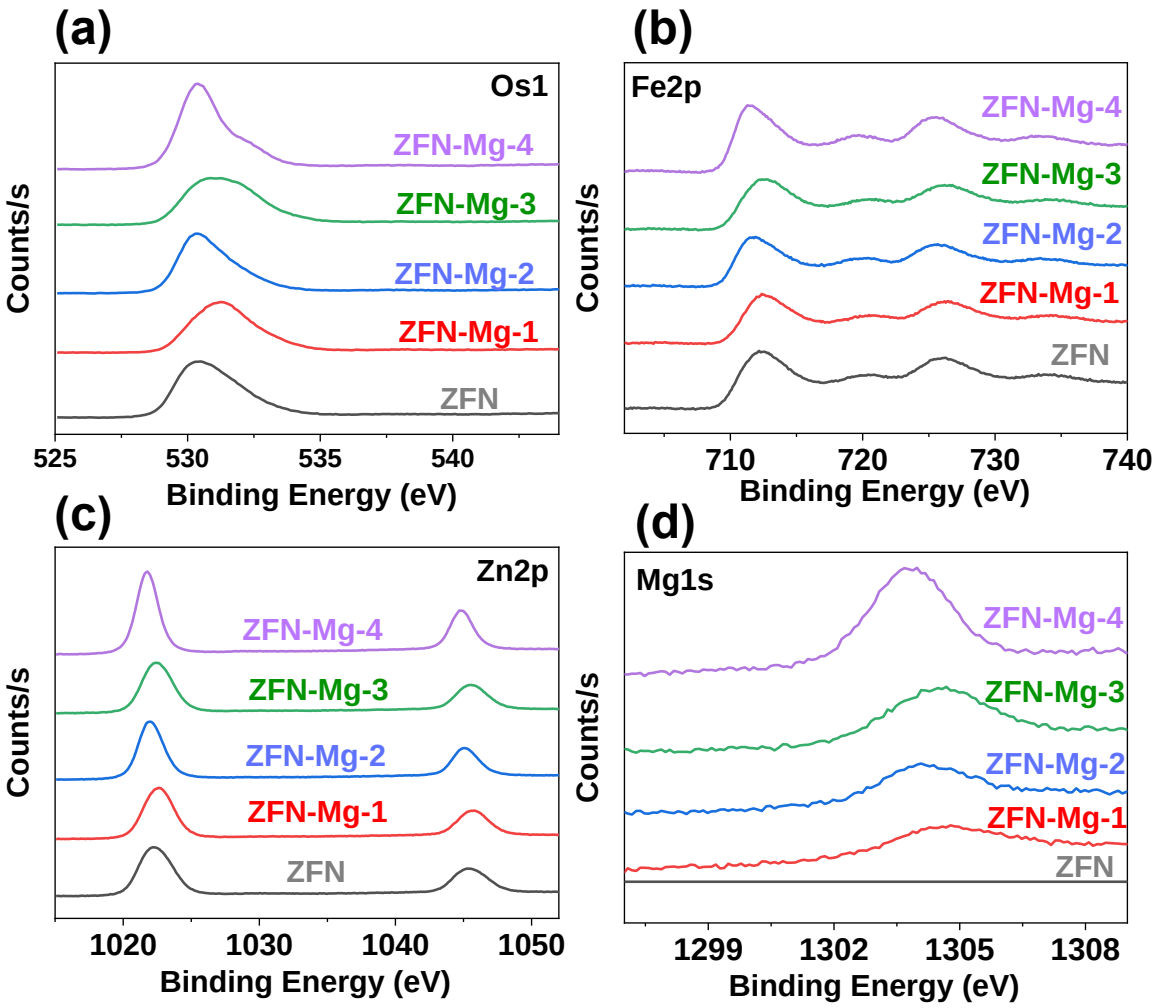

Figure 3. XPS views of (a)O1s, (b)Fe2p, (c)Zn2p and(d)Mg 1s for Mg doped $ZnFe_2O_4$ nanoparticles.

3.4. BET surface area

The Adsorption-desorption BET isotherm curves are analysed to determine the surface area and pore structure parameters of the prepared zinc ferrite samples (ZFN, ZFN-Mg-1, ZFN-Mg-2, ZFN-Mg-3, and ZFN-Mg-4). As shown in Figure 4 (a-e), all samples exhibit the same pattern of isotherm curves where an elevated H4 type hysteresis loop is observed at higher P/P_0, indicating a flatter shape of pores (Al-Najar et al., 2017). The calculated BET surface area is found to increase with Mg doping. The variation of the calculated value of BET surface area as function of Mg doping is shown on Figure 4 f, i.e., 28.4, 34.6, 38.9, 38.5, 39.3 m^2/g for ZFN, ZFN-Mg-1, ZFN-Mg-2 ZFN-Mg-3 and ZFN-Mg-4, respectively. The derivate surface areas *vs.* pore width graphs are shown as insets in Figure 4 (a-e) and the calculated pore size (PS) manifests a gradual decrease upon Mg doping, i.e., from 135.6 Å to 108 Å. Such variation in the surface area and porous structure is attributed to the doping process (Hareendran et al., 2022), that is expected to consequently affect the efficiency in the adsorption of heavy metals (Mariosi et al., 2020; M. Wang et al., 2021). As the grains and crystals of the prepared pure and Mg doped zinc ferrite samples manifest similar values, the increase in the surface area can be attributed to lower agglomeration that can be caused by doping as shown in recent reports (Keerthana et al., 2022).

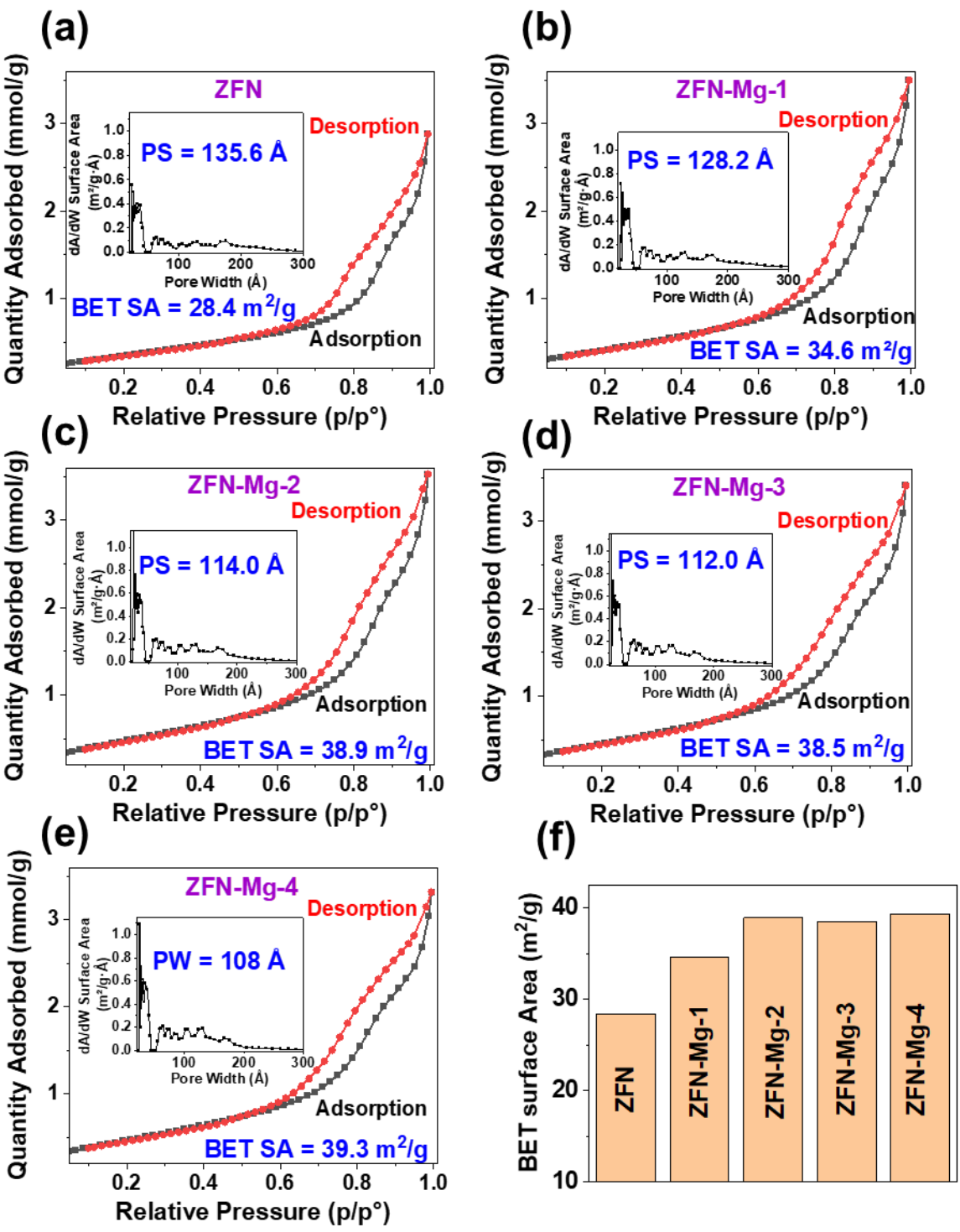

Figure 4. Adsorption-Desorption isotherms for (a) pure ZFN, (b) ZFN-Mg-1, (c) ZFN-Mg-2, (d) ZFN-Mg-3, and (e) ZFN-Mg-4.

3.5. Adsorption of heavy metals by Mg doped zinc ferrite nanoparticles

3.5.1. Effect of Mg doping on adsorption capacity and the role of hydroxyl group.

To determine the most efficient sample for the adsorption of Pb^{+2} ions, all the prepared samples have been tested for batch experiments under certain operating conditions. As presented in Figure 5 a, the obtained results reveal a significant enhancement in the adsorption capacity upon doping the zinc ferrite with Mg. The calculated adsorption capacity increases from 143 mg/g to 150 mg/g, reflecting a considerable increase only by doping the ferrite lattice by 2.5% Mg. With further doping, a slight increase in adsorption capacity is observed reaching a maximum of 153 mg/g for the 7.5% Mg doped sample (ZFN-Mg-3). Overall, all samples manifest excellent adsorption efficiencies of Pb^{+2} ions of more than 90% for pure zinc ferrite and 99.9 % for Mg doped samples. Such improvement in the adsorption efficiency can be directly correlated with the increase in the surface area induced by Mg doping (Mariosi et al., 2020)(M. Wang et al., 2021).

Moreover, the enhancement of the adsorption capacity can be related to the hydroxyl (OH-) surface group. Its role in the ferrite structure has been emphasised in the literature (A. Ivanets, et al., 2021), as the heavy metals ions onto ferrites particles' surface are mainly binding with this group. In Figure S2, the O1s XPS spectrum of all prepared ZFN samples has been fitted with three best gaussian curves which are related to O_2, H_2O and OH- groups. The OH- group abundancy can be related to the peak appearing between 531 and 532 eV, as reported in the literature (Wu et al., 2018). Comparing all samples, ZFN-Mg-3 demonstrates the highest OH- peak, which is related to the hight OH- percentage among all samples. Such change of OH- group in ZFN is caused by Mg doping, as Mg ions occupy the octahedral sites within the ZFN crystal lattice. The ZFN-Mg-3 shows the highest OH group abundancy as well as the highest adsorption capacity, which explains the mechanism of enhancing adsorption through doping process (Wu et al., 2018). As ZFN-Mg-3 sample exhibits the optimum adsorption efficiency of 152 mg/g with the highest BET surface area (38.5 m^2/g)

alongside the high abundancy of OH- surface groups as seen in Figure S2, therefore it has been used to perform further adsorption experiments.

3.5.2. The pH point of zero charge (PZC)

The pH PZC value of ZFN-Mg-3 is obtained from the intersection of ΔpH *vs.* initial pH plot, which is around 5.1, as shown in Figure 5 b. This indicates that the Mg doped zinc ferrite sample is positively charged in a solution pH lower than pH 5.1 and negatively charged in a solution pH higher than pH 5.1.

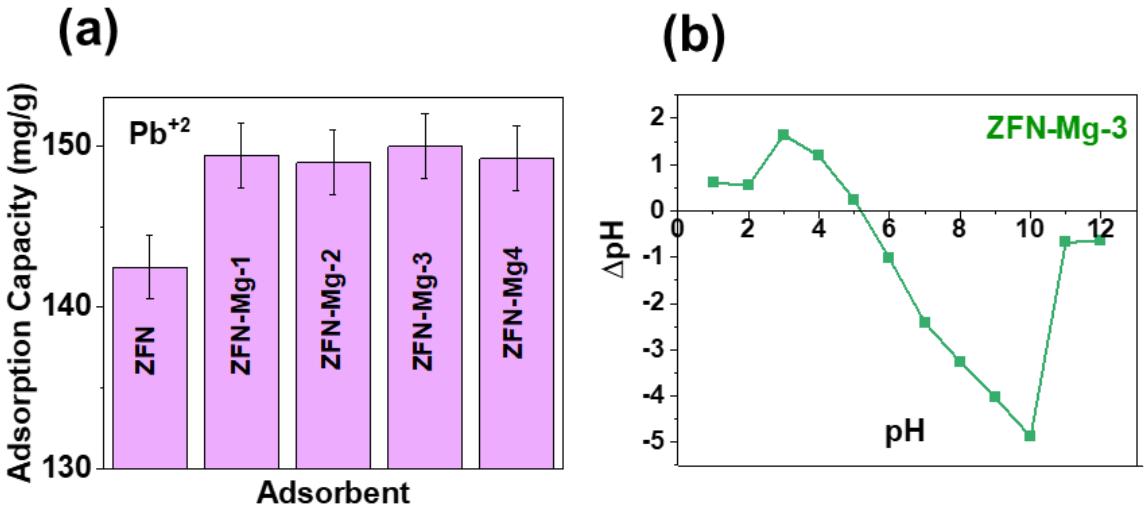

Figure 5. (a) Adsorption capacities for Pb^{+2} ions using Mg-doped $ZnFe_2O_4$ nanoparticles, (b) Zero-point charge of ZFN-Mg-3 sample at room temperature.

3.5.3. Individual adsorption of lead, cadmium, and copper ion by Mg doped zinc ferrite nanoparticles

The adsorption of the three heavy metals ions, Pb^{+2}, Cu^{+2} and Cd^{+2}, is investigated individually for the synthesised zinc ferrite doped with 7.5 % Mg (ZFN-Mg-3). The same experimental conditions have been applied for the three heavy metals ions experiments, i.e., initial metal concentration 60 mg/L, adsorbent amount 10 mg per 25 mL solution, pH=7, and temperature 25 °C.

The adsorption capacity is determined in different time intervals to assess the behaviour of the adsorbent toward the metal ions with time. Figure 6 (a-c) demonstrates the performance

of the ZNF-Mg-3 adsorbent toward Pb^{+2}, Cu^{+2} and Cd^{+2} ions, respectively. It is worth mentioning that the adsorption process of the three heavy metals present similar trend as the adsorption capacity increases considerably during the first 40 min reaching an equilibrium stage within 120 min.

The adsorption capacity shows the highest value with Pb^{+2} ions. As shown in Figure 6 a, the adsorption capacity of Pb^{+2} ions reaches 143 mg/g within only 30 min and no noticeable increase is further noticed at 60 and 120 min indicating that the adsorption equilibrium is attained. This is equivalent to 99.9% adsorption efficiency, where almost all Pb^{+2} ions have been adsorbed on the surface of the ZFN-Mg-3. Such performance, in term of adsorption capacity, adsorption efficiency, and contact time, is considered to be greater than other similar works in the literature. For example, nickel doped zinc ferrite adsorbent exhibited only 64.75 mg/g within 90 min toward Pb^{+2} ions (Ma et al., 2020). Copper magnesium ferrite showed 57.7 mg/g toward Pb^{+2} ions that is equivalent to 95% adsorption efficiency (Tran et al., 2020). While Mn dopped zinc ferrite/biochar composite showed a maximum adsorption capacity of 99.5 mg/g.

For Cu^{+2} ions (Figure 6 c), the adsorption capacity shows a rapid increase within the first 30 min reaching an amount of 117 mg/g. For longer contact time, the adsorption capacity reaches 125 mg/g at 60 min and remains almost steady until 120 min. This is equivalent to 86 % adsorption efficiency. In the other hand, Cd^{+2} seems to have the least adsorption affinity to ZFN-Mg-3 among the three metals. As shown in Figure 6 e, the adsorption capacity of Cd^{+2} starts with a gradual increase reaching 46 mg/g within 30 min and continue increasing reaching 61 mg/g and 77 mg/g at 60 and 120 min, respectively.

Furthermore, the effect of the initial concentration of the heavy metal ions is investigated individually for Pb^{+2}, Cu^{+2} and Cd^{+2} ions. Within the same amount of Mg doped zinc ferrite adsorbent (10 mg for 25 mL solution) the concentrations of the heavy metal ions are varied at 5, 15, 30, 45, 60, 100 and 200 mg/L. The residual concentration of heavy metal has been recorded after 120 min of contact time and the adsorption capacities are calculated. The effect of the initial concentration of the heavy metals on the adsorption capacities is shown in Figure 6 (b, d, f). Almost, equivalent effects are observed for all heavy metals, as the adsorption capacity increases with the initial concentration of metal ions in the aqueous

solutions. For the adsorption of Pb^{+2} ions (Figure 6 b), the recorded adsorption capacities are 12.49 mg/g, 37.36 mg/g, 72.82 mg/g, 106.65 mg/g, 143.25 mg/g, 227 mg/g and 462.5 mg/g, with respect to the above-mentioned concentrations, exhibiting a linear relationship. Alternatively, the effect of the initial concentration of Cu^{+2} ions on its adsorption capacity (Figure 6 d) seems to be less linear with the calculated adsorption capacities values 12.32 mg/g, 35.05 mg/g, 66.25 mg/g, 93.75 mg/g, 95 mg/g, 153.25 mg/g and 378.75 mg/g. A very similar reduction is observed in Figure 6 f, demonstrating the adsorption of Cd^{+2} ions with calculated adsorption capacity of 8.75 mg/g, 23.5 mg/g, 46.75 mg/g, 69.25 mg/g, 79 mg/g, 103.75 mg/g and 200.75 mg/g, corresponding to the above-mentioned initial concentrations.

In summary, the effect of contact time and the initial concentration of the adsorbate occur following similar trends agreeing with the nature of the adsorption process that is reported in the literature. The information obtained from these results is very essential for further analyses of the adsorption kinetics and isotherms, which will be presented and discussed in the following sections.

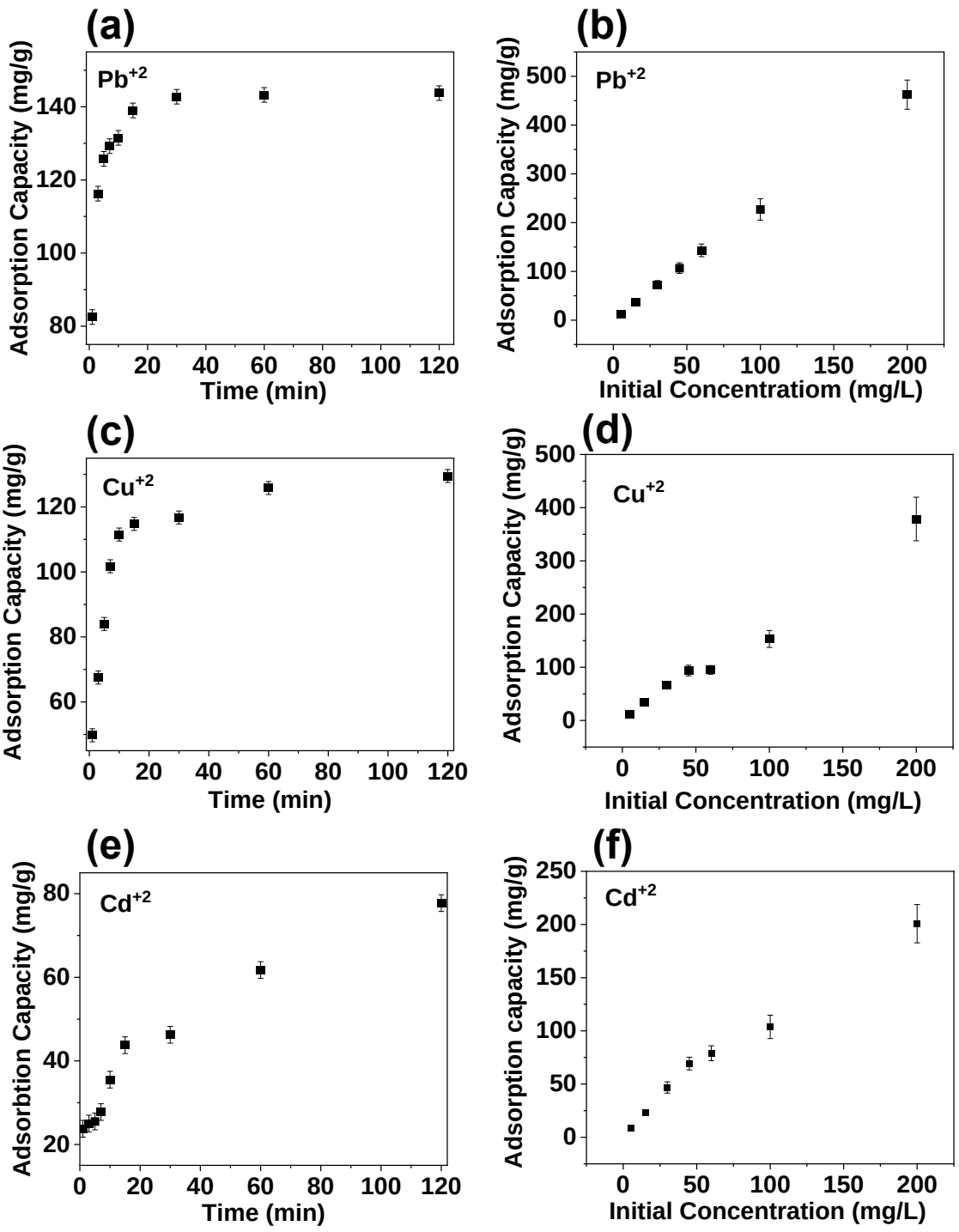

Figure 6. The calculated trends of the adsorption capacities vs contact time of (a) Pb^{+2}, (c) Cu^{+2} and (e) Cd^{+2} and vs the concentration of heavy metal pollutant concentration (b) Pb^{+2}, (d) Cu^{+2} and (f) Cd^{+2} using ZFN-Mg-3.

3.5.4. Adsorption kinetics

To investigate the kinetics models for the removal of Pb^{+2}, Cu^{+2} and Cd^{+2} ions by Mg-doped zinc ferrite nanoparticles, the kinetic experimental data have been assessed to fit the pseudo-first order and pseudo-second order kinetic models. The linear and non-linear forms of both equations are given in Table 2 along with the explanation of their parameters. Figure 7 presents the kinetic data of the individual heavy metal ions adsorption experiments fitted to the pseudo-first order and pseudo-second order equations, considering the linear forms for the two equations. To obtain the pseudo-first order parameters, ln ($q_e - qt$) is plotted *vs.* time, while the adsorption capacity q_t *vs.* time is plotted for the pseudo-second order fitting. The plotted data are subjected to a linear fit; hence, the reaction parameters are computed from the obtained values of the slope and the intercept of the fitted equations. K_1 and K_2 (min^{-1}) are the constants of the pseudo-first order and pseudo-second-order models, respectively, where K_1 indicates the rate of the adsorption reaction as a function of concentration whereas K_2 takes into account the adsorption capacity of the reaction (Sahoo & Prelot, 2020). The obtained values of slope, intercept, the calculated parameters, and the correlation coefficient (R^2) of the two kinetics models are presented in Table 2.

For the adsorption of Pb^{+2} ions, the kinetics data show a good fitting with the pseudo-first order as shown in Figure 7 a, with ($R^2 = 0.988$) and calculated (K_1=0.154 min^{-1}, q_e=48.09 mg/g). The data also reveal a better fitting for the second order model, as shown in Figure 7 b, with ($R^2 = 0.999$) and calculated (K_2=0.0096 min^{-1}, q_e=143 mg/g). Similarly, both kinetic models manifest good fitting to the data of the adsorption of Cu^{+2} ions (Figure 7(c-d)) as the pseudo-first order model is linearly fitted, with ($R^2 = 0.986$) and the calculated parameters (K_1=0.3 min^{-1}, q_e=109.9 mg/g). However, the kinetics parameters of the adsorption of Cd^{+2} ions reveal relatively lower fitting values as illustrated in Figure 7 (e-f) with R^2 =0.962 and R^2= 0.983 for the first and the second models, respectively. The first order model parameters are calculated as (K_1=0.03 min^{-1}, q_e = 64.1 mg/g), while the second order parameters are (K_2 = 0.0008 min^{-1}, q_e = 79 mg/g).

In summary, both models show good linear fittings with the experimental kinetic data for the three heavy metals ions. The first order constant (K_1) is found to be highest for Cu (0.3 min^{-1}) in comparison with Pb^{+2} (0.154 min^{-1}) and Cd^{+2} (0.03 min^{-1}), as it depends on the

concentration and time only. However, when the adsorption capacity is taken into account in the second kinetic model, the Pb^{+2} shows the highest constant (K_2) among the three models (K_2 = 0.0096 min^{-1}). The compatibility for both models to the adsorption of the three metal ions indicates that the reaction between the Mg doped zinc ferrite adsorbent and the heavy metal ions is mainly controlled by ions' exchange and surface precipitation as stated in previous studies (Tho et al., 2021).

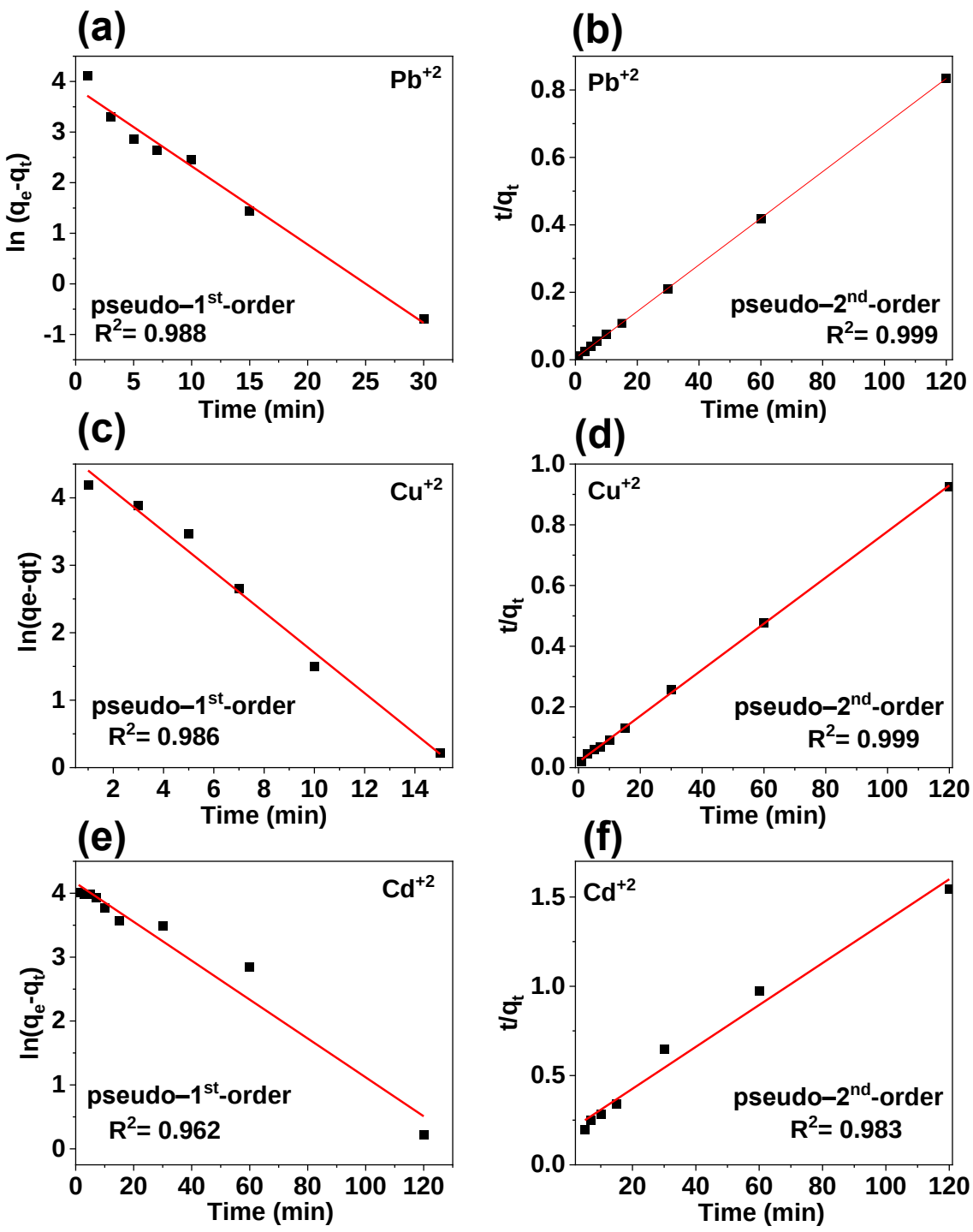

Figure 7. Pseudo first and second order adsorption kinetics for (a,b) Pb^{+2} ions (c,d) Cu^{+2} ions and (e,f) Cd^{+2} ions.

3.5.5. Adsorption isotherms

The experimental data when varying the initial concentration of heavy metal ions are employed to determine the compatibility of the individual adsorption of Pb^{+2}, Cu^{+2} and Cd^{+2} ions on the ZFN-Mg-3 adsorbent to Langmuir and Freundlich isotherm models. The Langmuir model assumes that the adsorption process occurs on the homogeneous surface of the adsorbent creating a monolayer surface of the adsorbate while the Freundlich model refers to describe heterogeneous systems (multilayer) (J. Wang & Guo, 2020). The nonlinear and linear forms of the two models are shown in Table 1. The linear form of the two models has been applied for fitting the experimental data in this study. For Langmuir model, based on the equation given in Table 1, Log C_e (Equilibrium concentration) has been plotted *vs.* Log q_e (equilibrium capacity). Then the plot is fitted to the linear form of the equations and the Langmuir constant K_L and the maximum adsorption capacity q_m are computed from the obtained slope and intercept, respectively. To further investigate the adsorption process of the three heavy metals, the adsorption concentration data have been also fitted with the linear form of the Freundlich equation given in Table 1. In Figure 8, the plots of the linear forms of both Langmuir and Freundlich models are shown along with the fitting lines, for the adsorption of Pb^{+2}, Cu^{+2} and Cd^{+2} ions by the Mg-doped zinc ferrite adsorbent. The calculated parameters of Langmuir and Freundlich models are given in Table 3.

Considering Pb^{+2} ions, the adsorption data manifests a good fit with the linear equation giving a correlation coefficient of R^2= 0.899. The calculated Langmuir constant is K_L=0.748 L/mg while the maximum adsorption capacity is q_m=243.9 mg/g. The Freundlich model shows a better agreement with the Pb^{+2} adsorption data as the correlation coefficient reaches higher value of R^2=0.954. The calculated Freundlich constant and the n parameter are 101.3025 L/mg and 2.53, respectively.

In the case of Cu^{+2} ions, the Langmuir and Freundlich fitting is reported in Figure 8 (c and d). It can be observed that both isotherm models fit well the experimental data with a close correlation coefficient of R^2=0.913 and R^2=0.916, respectively. The corresponding calculated parameters are: K_L= 0.241 L/mg and q_m=149.9 mg/g; K_F=37.26 and N=2.24.

For Cd^{+2} ions, the experimental data indicate the occurrence of both Langmuir and Freundlich models, as shown in Figure 8 (e and f) with a similar correlation coefficient R^2 = 0.977 representing the highest among the three metals ions. The calculated models' parameters are found to be K_L = 0.0396 L/g and q_m = 150.1502 mg/g; K_F=7.4798 and N=1.437. In comparison to Pb^{+2} and Cu^{+2} adsorption, the Freundlich manifests the lowest values.

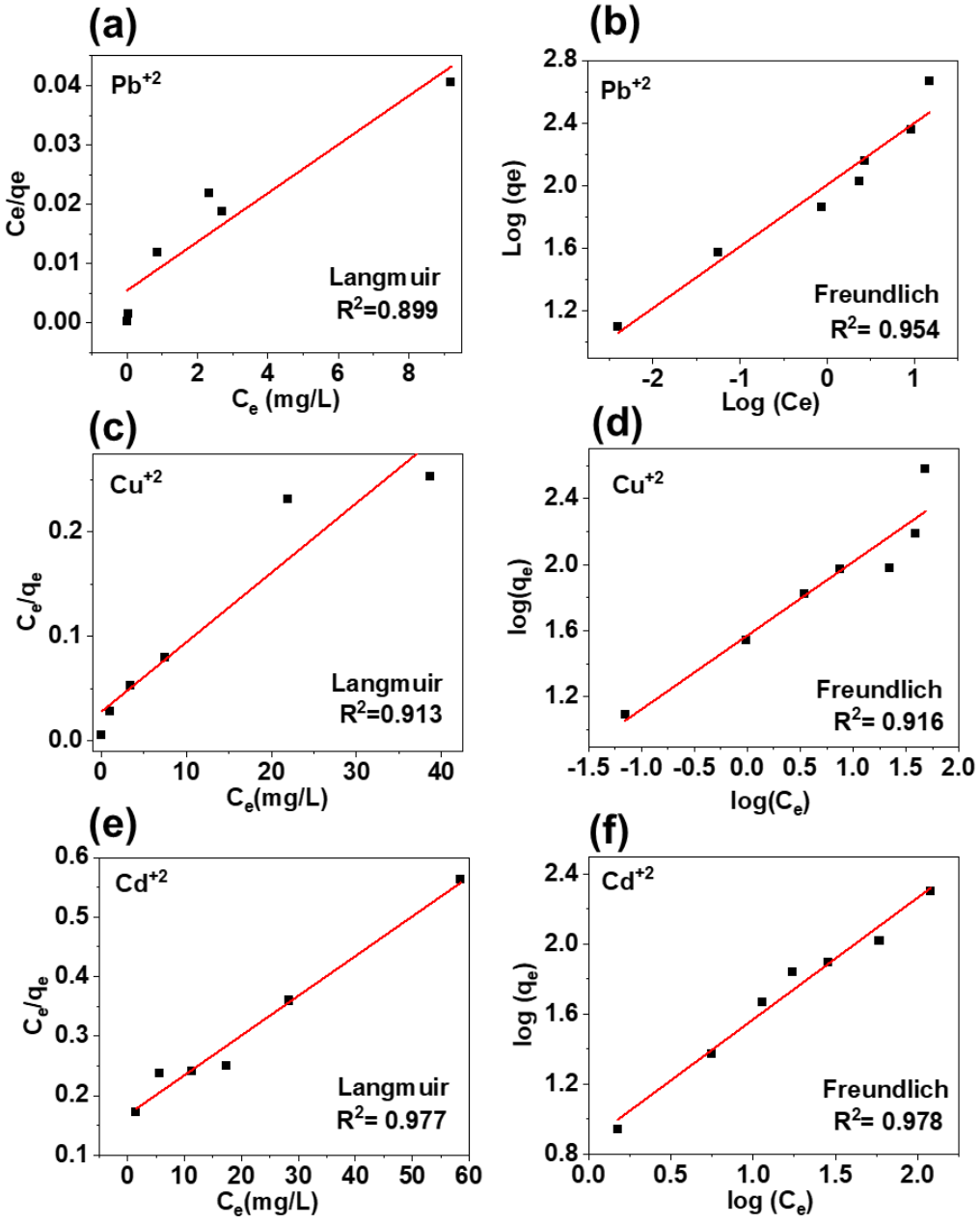

Figure 8. Freundlich and Langmuir adsorption isotherms for (a,b) Pb^{+2} ions; (c,d) Cu^{+2} ions; and (e,f) Cd^{+2} ions.

Table 1: Linear and non-linear equations for adsorption kinetics and isotherm models applied in this work (Punia et al., 2022)**.**

Model	Equation		Parameters
	Linear	Non-linear	
Pseudo first order kinetic	$\ln(q_e - q_t) = \ln q_e - K_1 t$	$q_t = q_e(1 - e^{K_1 t})$	K_1 (min^{-1}) is the adsorption rate constant of the first-order kinetic studies, q_e (mg/g) is the adsorption capacity at equilibrium, q_t (mg/ g) is the amount adsorbed in time t
Pseudo second order kinetic	$\frac{t}{q_t} = \frac{1}{K_2 q_e^2} + \frac{t}{q_t}$	$q_e = \frac{q_e^2 K_2 t}{1 + q_e K_2 t}$	K_2 (g/mg min) is the rate constant from second order kinetic studies, q_t (mg/g) and q_e (mg/g) are the adsorption capacities at time t (min) and equilibrium, respectively.
Langmuir	$\frac{C_e}{q_e} = \frac{1}{q_m K_L} + \frac{C_e}{q_m}$	$q_e = \frac{q_m K_L C_e}{1 + K_L C_e}$	q_e (mg/g) is the adsorption capacity at equilibrium; C_e (mg/L) is the concentration of metal ions in contaminated solution at equilibrium; q_{max} (mg/g) is the maximum adsorption capacity; K_L (L/mg) is Langmuir constant
Freundlich	$\ln q_e = \frac{1}{n} \ln C_e + \ln K_F$	$q_e = K_F C_e^{1/n}$	q_e is the adsorption efficiency at equilibrium; C_e is the equilibrium/final concentration of metal ions in aqueous solution; K_F [(mg/g) $(mg/L)^{-1}$/n] is the Freundlich constant, and n is a dimensionless parameter

Table 2. Kinetics parameters of the adsorption of Pb^{+2}, Cu^{+2} and Cd^{+2} using Mg-doped zinc ferrite nanoparticles.

	P-1st order					P-2nd order				
	slope	**intercept**	**q_e**	**K_1**	**R^2**	**slope**	**intercept**	**q_e**	**K_2**	**R^2**
Pb^{+2}	-0.154	3.873	48.08643	0.154	0.988	0.00691	0.00509	143	0.009607	0.999
Cu^{+2}	-0.3	4.7	109.9472	0.3	0.986	0.00759	0.0186	95	0.005957	0.999
Cd^{+2}	-0.03043	4.16105	64.13883	0.03043	0.962	0.01173	0.1912	79	0.000838	0.983

Table 3. Isotherms parameters of the adsorption of Pb^{+2}, Cu^{+2} and Cd^{+2} using Mg-doped zinc ferrite nanoparticles.

	Langmuir					Freundlich				
	slope	**intercept**	**q_m**	**KL**	**R^2**	**slope**	**intercept**	**K_F**	**N**	**R^2**
Pb^{+2}	0.0041	0.00548	243.9024	0.748175	0.899	0.3949	2.00562	101.3025	2.532287	0.954
Cu^{+2}	0.00667	0.0276	149.925	0.241667	0.913	0.44555	1.5713	37.2649	2.244417	0.916
Cd^{+2}	0.00666	0.16792	150.1502	0.039662	0.977	0.6956	0.87389	7.4798	1.437608	0.978

3.5.6. Effect of pH on the adsorption of lead, cadmium, and copper ions

The effect of pH on the adsorption of Pb^{+2}, Cu^{+2}, and Cd^{+2} has been investigated within the pH range from 1 to 8 by using ZFN-Mg-3 adsorbent under optimized experimental conditions (initial concentration 40 mg/L, nanoparticles initial concentration 10 mg per 25 mL solution, contact time is 60 min). The recorded adsorption capacities are shown in Figure 9 (a, b, c). The adsorption of the three heavy metals by Mg-doped zinc ferrite sample reveals a distinct trend when varying the pH values as illustrated in Figure 9. For the adsorption of Pb^{+2} ions (Figure 9 a), the adsorption capacity records a dramatic rise at pH 3 as it increases from 3.7 mg/g up to 66.7 mg/g. At pH 5, the adsorption capacity drops markedly to 9.6 mg/g while it raises slightly to 19.9 and 16.9 mg/g at pH 7 and 8, respectively.

Different behaviour is observed for the adsorption of Cu^{+2} when varying the pH value as illustrated in Figure 9 b. A gradual increase of the adsorption capacity is noted when the pH changes from 1 to 5, i.e., 1.75 mg/g at pH 1, 37.5 mg/g at pH 3, reaching its maximum 52 mg/g at pH 5. Further rise in the pH value (7 and 8) results in a gradual decline of the adsorption capacity to 39.7 and 19.7 mg/g respectively.

In the other hand, as depicted in Figure 9 c, the adsorption capacity of Cd^{+2} ions reach its lowest value of 5 mg/g at pH 1 and then increases gradually to 14.75 at pH 3, 39.7 mg/g at pH 5, to finally reaching its maximum 65.2 mg/g at pH 7. Surprisingly, further increase of pH to 8, is followed by a sharp decline in the adsorption capacity by halve, i.e., 32 mg/g.

The different interactions' tendencies of the three metals toward adsorption in different pH media has been reported lately. This was associated with the existence of different states of metal in different aqueous environments (Król et al., 2020; Miranda et al., 2022; Tho et al., 2021). Pb^{+2}, Cu^{+2} and Cd^{+2} ions acquire different chemical states when the pH is varied (Abuhatab et al., 2020). In general, at high acidic environment (low pH), the existing of hydrogen atom may block the adsorption active sites while at alkaline environment (high pH), the metal ions can interact with OH- groups forming hydroxyls such as $Pb(OH)_2$. This would lower the concentration of heavy metals in their single ionic state leading to a lower adsorption capacity (Çelebi et al., 2020). Another important aspect to be considered reflects

the charge of the ZFN-Mg adsorbent that varies with pH. As shown previously (Figure 5 b), the obtained zero-point charge of ZFN-Mg-3 adsorbent occurs at pH 5. In general, if the zero-point charge occurs at less than pH 7, then the surface is negatively charged (Tengvall, 2011). This would possess more adsorption affinity of positively charged heavy metal ions in the acidic medium.

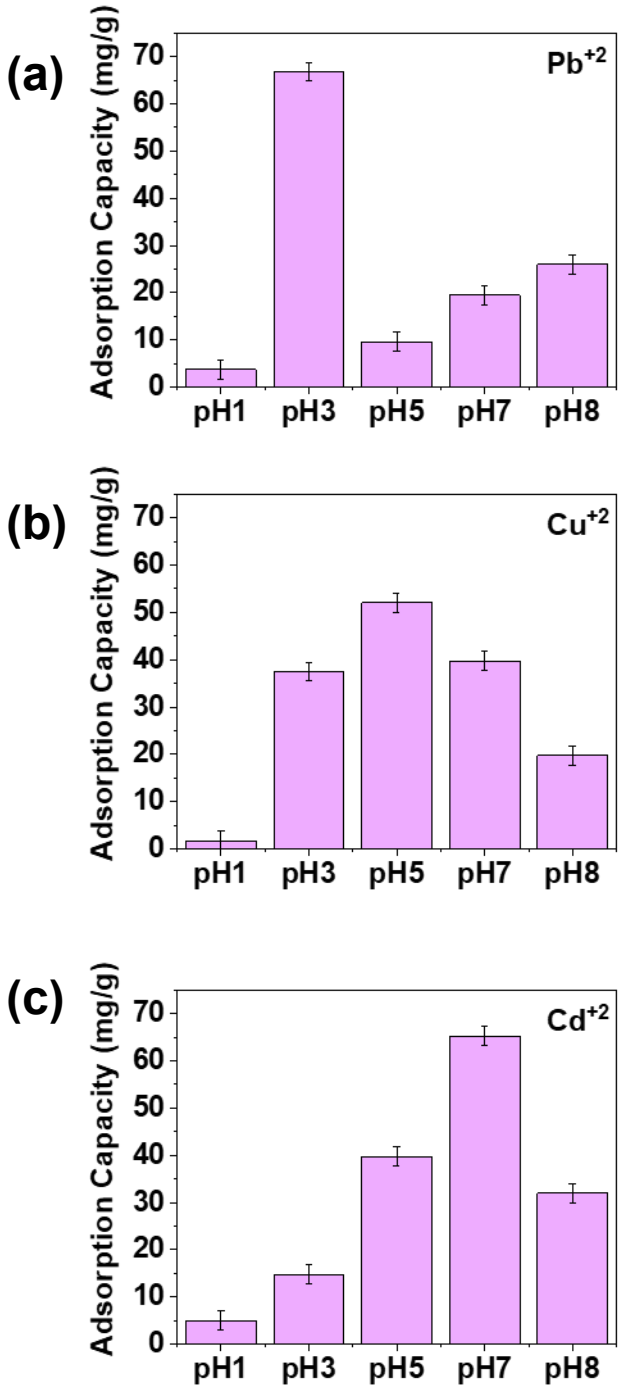

Figure 9. pH effect on the adsorption capacities of (a) Pb^{+2}, (b) Cu^{+2}, and (c) Cd^{+2} using ZFN-Mg-3 adsorbent.

3.5.7. Simultaneous adsorption of Lead, Cadmium and Copper ions in aqueous solution and seawater.

In real life, toxic metals exist together in different conditions of aqueous environments, along with other substances. To investigate the efficiency of the prepared Mg-doped zinc ferrites in situations closer to the real-life conditions, the adsorption experiments were performed with the three previous tested metals (Pb^{+2}, Cu^{+2}, Cd^{+2}) together in distilled water as well as different samples of seawater.

The competitive adsorption capacities and efficiencies of the three metal ions are recorded in distilled water and other seawater samples collected from different points in Bahrain seashores, see Figure 10. In distilled water, the adsorption capacity of each metal is found to be reduced in comparison with their respective individual adsorption capacity. Herein, it is important to highlight that the active sites present on the adsorbent surface are limited to certain concentrations of metal ions. As shown in Figure 10, a significant affinity of the adsorbent toward Pb^{+2} ions is confirmed in distilled water, where the calculated adsorption capacity is 85 mg/g in comparison with only 20 mg/g and 25 mg/g for Cu^{+2} and Cd^{+2} ions, respectively. This is equivalent to 85 %, 19.5 % and 16.6 %, with respect to the above metal ions order. The difference in adsorption affinity toward different metals was previously reported (Shan et al., 2020). This is may be due to the presence of several types of sorption centers with different affinities to toxic metal ions (A. Ivanets, Prozorovich, Kouznetsova, et al., 2021b). Moreover, the three heavy metal ions exist in different forms in certain chemical environments (i.e., certain pH values) as discussed previously and hence the initial concentration of the metal ions will be affected, which accordingly affect its adsorption capacity. Therefore, the adsorption efficiency is calculated too to provide more information about the adsorption process.

Furthermore, the competitive adsorption experiments of the three metals have been also conducted in real seawater samples. All samples have almost similar pH = 8 and conductivity. The results shown in Figure 10 reveal a substantial reduction in the adsorption capacities and efficiencies for the three metals in sweater samples. For the first sweater sample (SW1, collected near Al-Dar Islands in the Northeast of Bahrain), the calculated adsorption capacities and adsorption efficiencies are 12.5 mg/g (7.5 %), 2.5

mg/g (1.9 %) and 7.5 mg/g (5 %) for Pb^{+2}, Cu^{+2} and Cd^{+2}, respectively. The second seawater (SW2) sample (collected near Al-Hidd industry area at the far Northeast of Bahrain), the adsorption capacity also shows its highest affinity toward Pb^{+2} ions, i.e., 12.5 mg/g (7.1%). In the other hand, the adsorption capacities of Cu^{+2} and Cd^{+2} ions are found slightly smaller than Pb^{+2}, i.e., 10 mg/g (6.5 %) and 7.5 mg/g (4.9 %), respectively. Interestingly, for the third sample (SW3, collected from Al-Dur seashore that is located in the Southeast of Bahrain), the adsorption capacities manifest a considerable increase, the calculated adsorption capacities are almost similar for the three heavy metals, i.e., 27.7 mg/g (15.4 %) for Pb^{+2}, 22.5 mg/g for Cu^{+2} and 22.5 mg/g for Cd^{+2}.

Essentially, the adsorption performance of Mg-doped zinc ferrite nanoparticles toward the three metal ions have shown a considerable decline in seawater samples. This can be explained by the chemical complexity of seawater compared to distilled water, as various metals and salts coexist creating a strong ionic strength within the solution as well competing with other ions and blocking the adsorption active sites on the adsorbent surface. This was already confirmed by previous reports that investigated the effect of salts and ionic strength on the adsorption process (A. Ivanets, Prozorovich, Kouznetsova, et al., 2021a)(Tang et al., 2019). Such results provide insights about the importance of considering the surrounding environment during the investigation of new adsorbents as it has major effects on the adsorption efficiency. Harsh environmental conditions, such as the high salinity that exists within the Arabian gulf water, creates a great challenge for heavy metal removal process.

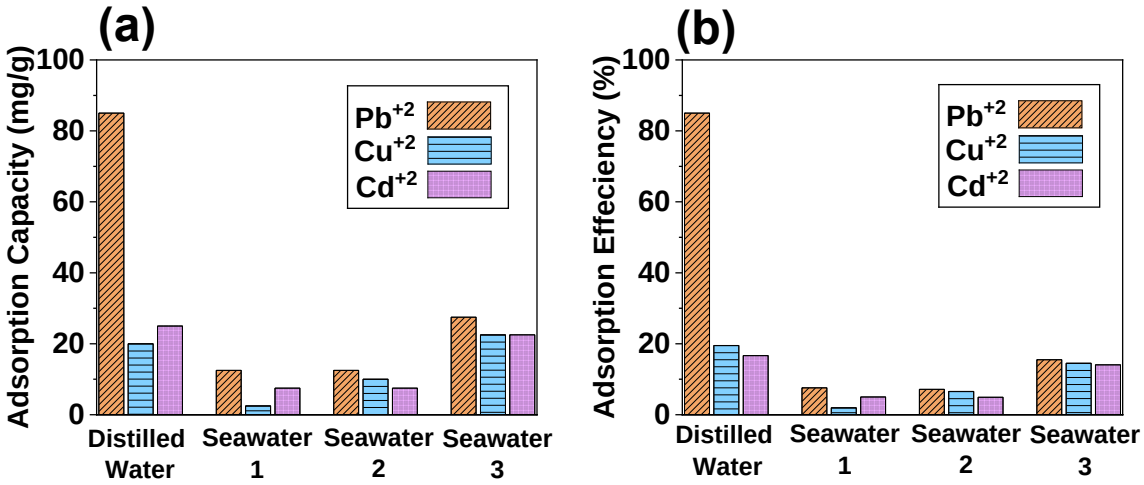

Figure 10. (a) Simultaneous adsorption capacity and (b) adsorption efficiency of Pb^{+2}, Cu^{+2} and Cd^{+2} ions in distilled water and seawater samples.

3.5.8. Comparison with the literature

In comparison to other adsorbents reported in the literature for heavy metal removal, the prepared Mg doped zinc ferrites demonstrate significant performance in term of adsorption capacity, efficiency, and reaction time. The above parameters have been used as indicators in assessing the adsorption performance of the newly designed adsorbents. The obtained results clearly indicate that the adsorption capacity depends on the mass of the adsorbent (dose) and the sample size with respect to the concentration of the pollutants. The adsorbent with higher mass would lead to relatively higher adsorption capacity, based on equation 1, the common equation applied to calculate the adsorption capacity. Nonetheless, it cannot be considered as the only indication of a good adsorption performance. Furthermore, the removal percentage calculation does not include the experimental parameters and does not account for the adsorbent properties. It is essential to combine different aspects when evaluating the adsorption efficiency to obtain an integrated overview about certain adsorbent. In this work, we have provided the adsorption capacity, the adsorption efficiency (percentage of removed pollutant), and the reaction time to elucidate a more comprehensive evaluation for the adsorption performance. It is very important to consider the wide variation of the experimental parameters which are one of the main influencing criteria of the adsorption performance.

When comparing our Mg-doped zinc ferrite adsorbent with other adsorbents applied recently in the literature for the removal of heavy metals from aqueous solutions, we have considered all the previous aspects. As per our search in the literature, we have noticed that the removal percentage and adsorption capacity were not mentioned cooperatively together in some published work. Hence, we have compared our work with the available information provided in the latest research articles. Table 4 includes a summary of previous works with the important parameters that reflect the adsorption performance. The selected articles were based on the type of adsorbent as we have selected similar ferrite nanoparticles with zinc and magnesium contents, that have been applied for heavy metal removal. Previous report has shown that MgO-Fe_2O_3 nanoparticles can be applied successfully in the removal of Cd^{+2} ions (Bououdina et al., 2019) with an adsorption capacity of 75.25 mg/g and a reaction time of 12 h. The same samples were also applied for Ni^{+2} ions removal with a capacity of 96.45 mg/g in 12 h.

Nowadays, researchers are aiming to create more powerful ferrite adsorbent by investigating multiple and competitive adsorption that occur in shorter time with high efficiency. Recent studies showed that synthesized nickel Ferrite nanoparticles have achieved relatively good efficiency reaching 89%, 79% and 87% for individual adsorption of Cr^{+3}, Pb^{+2} and Cd^{+2} within a moderate reaction time of 120 min (Khoso et al., 2021). However, when looking at the adsorption capacities, the values were found similar for the three metals with a very low average of 20 mg/g. The surface area and the porosity of the adsorbent were not investigated. The TEM showed random particle size distribution (Khoso et al., 2021). Moreover, zinc ferrite nanoparticles were incorporated with carbon nanotubes to give an excellent performance in the removal of Hg^{+2}, Pb^{+2}, Cd^{+2}, and Sn^{+2} with an efficiency of above 95 % in a very short time of 20 min for all metal ions (Adam et al., 2021), nevertheless, the adsorption capacities were not given in this work. The BET surface area was not investigated in both above-mentioned works, which makes it difficult to correlate the performance to the physicochemical properties of the applied adsorbents.

Furthermore, other studies that applied metal doping to zinc ferrite have used a larger weight percentage amount (more than 20%), in comparison with our work that applied small weight percentage (less than 10%). Some work investigated the zinc atom

occupancies within A and the B sites of the ferrite structure and its effect on the adsorption capacity of Arsenic As^{+4} (Tatarchuk, Shyichuk, et al., 2021). Different samples of doped and pure cobalt and zinc ferrite were investigated for Pb^{+2} ions removal. The pure zinc ferrite showed the highest adsorption capacity of 270.3 mg/g but in much longer reaction time of 24 h, while other doped samples performance was almost within the same contact time. In general, 24 h can be is considered as a long reaction time in comparison with other works mentioned in Table 4. This study also revealed that the heterogenous structure and doping would not necessarily enhance the adsorption performance. The grain size of all samples were almost similar, while the porosity and surface area were not investigated (Tatarchuk, Shyichuk, et al., 2021). Therefore, more in-depth and breadth studies are needed to have more comprehensive explanation about the correlations between structural, microstructural, and subsequently the physicochemical properties and their influence on the adsorption performance and involved mechanisms. The same research group showed a considerable investigation of the effect of doping ferrite nanoparticles including zinc and magnesium ferrites (Tatarchuk et al., 2020; Tatarchuk, Myslin, et al., 2021).

As per to our search in the literature, the previous group provided good investigation among few articles that considered metal doping ferrites for multiple heavy metals adsorption applications, which are addressed in Table 4. The main difference between our work and the previous work is that the metal doping has been applied within a smaller weight percentage alongside broad characterizations which helped the to correlate particle size, porosity, and surface with the adsorption performance. Comparing the performance of our synthesised Mg doped zinc ferrite nanoparticles with adsorbents having similar crystal structure, our samples have shown great performance in term of adsorption capacity (maximum 143.3 mg/g for Pb^{+2}), removal efficiency (99.9 % for Pb^{+2}) and reaction time (equilibrium reached within only 30 min). Such performance can be related to the high surface area, small pores (high porosity), surface properties (charge and adsorption sites).

1029 **Table 4. Comparison of simultaneous adsorption capacities in the literature and the current work.**

NPs applied	Heavy metals	Adsorption Capacity and percentage %	Experimental Parameters	Ref
$Mg_xZn_{x-1}Fe_2O_4$ x=0.025, 0.05, 0.075 and 0.1)	Individual and simultaneous adsorption of Pb^{+2}, Cu^{+2} and Cd^{+2}	Max results obtained at: Pb^{+2} – 143.3 mg/g (99.9 %) Cu^{+2} – 117 mg/g (86%) Cd^{+2} – 77 mg/g (50%)	pH 3–7, dose: 60 mg and contact time: 120 min)	This work
$NiFe_2O_4$	individual adsorption of Cr^{+2}, Pb^{+2} and Cd^{+2}	89%, 79% and 87%	pH 3–7, dose: 10, 20, 30, 40 and 50 mg and contact time: 30, 60, 90, and 120 min	(Khoso et al., 2021)
$MgO{\cdot}Fe_2O_3$	Cd^{+2}	75.25 mg/g	10 ± 0.1mg of adsorbent to 25 ml pH=7.0 dose of Ni^{+2}, Cd^{+2} and Cr^{+6} of 125, 83 and 105 mg/L, contact time 12 h	(Bououdina et al., 2019)
$ZnFe_2O_4$-carbon nanotube (CNT) adsorbent	Pb^{+2} and Cd^{+2}	97–99% of the heavy metal content within 20 min	10–50 mg; metal ion concentration, 20 mg/100 mL; pH, 2–8; time, 5–20 min	(Adam et al., 2021)
$CoxZn_{1-x}Fe_2O_4$ m (x= 0.4, 0.6, 0.8 and 1.0)	Pb^{+2}	Maximum at x= 1.0, 270.3 mg/g	initial concentration of Pb^{2+} = 17 mg/L; volume of Pb^{2+}solution = 50 mL; mass of the adsorbent = 2 mg; agitation time = 24 h; pH= 7).	(Tatarchuk, Shyichuk, et al., 2021)
$Mg_{1-x}Zn_xFe_2O_4$ (x= 0.4, 0.6, 0.8 and 1.0)	Cr^{+4} and Ni^{+2}	30.49 mg/g	temperature 25 °C and neutral pH. The ferrite samples with an exact mass of100mg were added to exact volumes (25 mL) 5 to 50 mg/L. The obtained for 24 h at room temperature. T	(Tatarchuk, Myslin, et al., 2021)
$Mg_{1-x}Zn_xFe_2O_4$ (where x = 0.4, 0.6, and 0.8)	Sr^{+2}	Maximum at x=0.6 adsorption capacity of 74 mg/g	by shaking 100 mg adsorbent 6 h at 22 °C.	(Tatarchuk et al., 2020)

$MgFe_2O_4$	Co^{2+}, Mn^{+2}, Ni^{2+} and Cu^{2+}	Co^{2+} (2.30 mmol g^{-1}) Mn^{2+} (1.56 mmol g^{-1}) Ni^{2+} (0.89 mmol g^{-1}) Cu^{2+} (0.46 mmol g^{-1})	0.04 g of sorbent ,10.0 mL solution (V/m = 250 mg L^{-1}; pH = 5.0 with, contact time: 90 min)	(A. I. Ivanets et al., 2018)

3.5.9. Recyclability of Mg-doped zinc ferrite adsorbent

The recyclability of Mg-doped nanoparticles for the adsorption of Pb^{+2} ions has been examined through several cycles. The filtered nano adsorbents are subjected to washing with distilled water and drying in oven after each adsorption cycle. A repetitive procedure is applied for five cycles and the adsorption capacity is calculated. The resultant adsorption capacities are shown in Figure 11 a. Initially, the adsorption capacity reaches 149.6 mg/g with a removal percentage of Pb^{+2} ions of 99.9%. In the second cycle, the capacity starts to decline up to 141.5 mg/g. For the rest of the cycles, a slight decrease is noticed as the adsorption capacity reaches 132.1 mg/g, 110.8 mg/g and 99.8 mg/g. In summary, the adsorption capacity of Mg-doped zinc ferrite toward Pb^{+2} ions decrease gradually following the repetitive treatment and reuse reaching a 33.1% reduction in the fifth cycle. The creation of new -OH adsorption sites in the Mg-doped zinc ferrite structure may be affected by several factors such as the nature and concentration of the solution (A. I. Ivanets et al., 2019).

Moreover, the nanoadsorbent has shown high stability in terms of particle morphology, crystal structure, and atomic structure. TEM images of the filtered and dried adsorbent powder after the adsorption process (Figure 11 b) indicates that the particle morphology and size besides the crystal fringes appear unmodified in comparison to the pristine Mg-doped zinc ferrite before adsorption. The XRD patterns of Mg-doped zinc ferrite adsorbent before and after the adsorption of Pb^{+2} ions process confirms the structure stability, as shown in Figure 11 c. Only the peaks corresponding to the pure spinel phase with a cubic crystalline structure remain apparent. Besides, new peaks with varying intensity emerge upon the adsorption with Pb^{+2} ions, located at 2θ = 24.7°, 27.2°, 34.1°, 40.3°, 44.2°, and 49.0°. Meanwhile, it is noticed that the peaks related to the pure zinc ferrite phase remain unaffected in terms of position and intensity. This indicates the inclusion of Pb^{+2} ions within the nanostructure and confirms the attachment between the adsorbent and the adsorbate. Furthermore, the FTIR spectrum of the zinc ferrite adsorbent was also recorded before and after Pb^{+2} adsorption, as shown in Figure 11 d. In addition to the main bands of the spinel ferrite cubic structure, a small peak emerges at 676.9 cm^{-1} alongside a sharp peak 1040 cm^{-1}. This indicates the formation of a new bond between Pb^{+2} ions and the functional groups present at the surface of Mg-doped ferrite nano adsorbent.

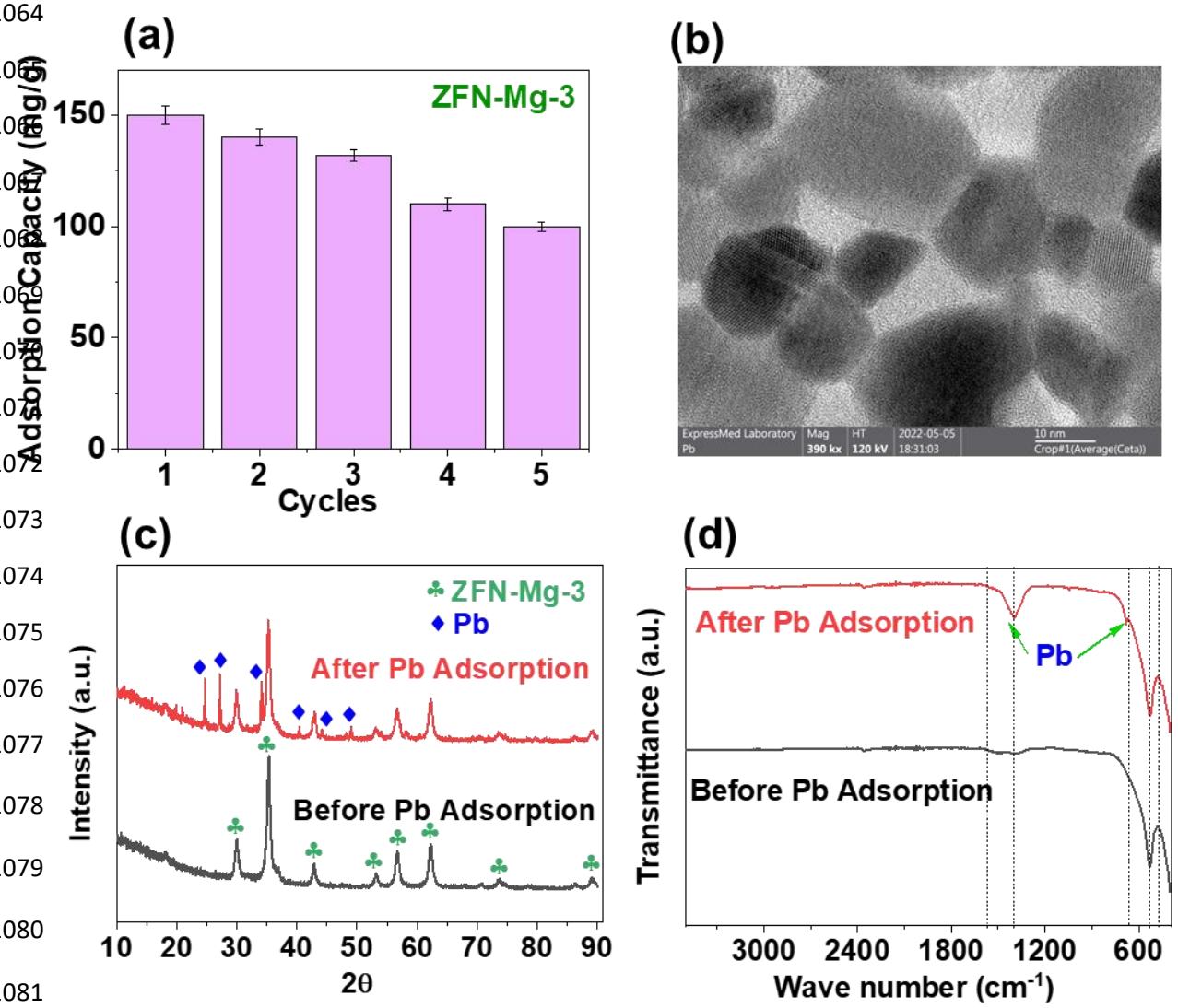

Figure 11. (a) adsorption capacity of Pb^{+2} ions using ZFN-Mg-3 sample over five cycles, (b)TEM image of ZFN-Mg-3 sample after adsorption process, (c) XRD patterns and (d) FTIR spectra for ZFN-Mg sample before and after adsorption of Pb^{+2} ions.

4. Conclusion

This research work provides insights on the influence of zinc ferrite nanoparticles' crystal lattice enhancement, through Mg doping, on heavy metals removal. The synthesized powdered samples were subjected to morphological, structural, and physicochemical characterization by TEM, XRD, FTIR, Raman spectroscopy, XPS, and BET. Small amount of Mg doping confirmed an enhancement in the surface area and the porosity, which subsequently affected the adsorption capacity of Pb^{+2}, Cu^{+2} and Cd^{+2} heavy metal ions. The synthesized ferrite nanoparticles exhibited a conventional adsorption behavior toward the three metal ions, as it was affected by the operating paraments such as contact time, concentration of metal ions, and pH of the solution. The adsorption data showed good agreement with pseudo-first order and pseudo-second order kinetic models. Similarly, both Langmuir and Freundlich isotherms successfully fitted the adsorption data. Moreover, Mg-doped zinc ferrite nanoparticles manifested considerable simultaneous adsorption behavior for (Pb^{+2}, Cu^{+2}, Cd^{+2}) with high selectivity toward Pb^{+2} ions. The simultaneous adsorption process was further investigated in seawater samples and indicated a major influence of the surrounding environment and the nature of the medium on the adsorption process. Finally, Mg- doped zinc ferrite nanoparticles showed relatively small decline in the adsorption capacity following five repetitive cycles. A high stability in terms of crystalline structure and particles morphology/size were confirmed by XRD, FTIR, and TEM. Such complementary analyses revealed the great potential of enhanced and highly crystalline ferrite structure in the adsorption of multiple heavy metals ions within harsh environmental conditions. Further investigations in applying another variety of heavy metals ions, different doping conditions to the ferrite structure, and different aqueous samples, are essential to strengthen research in this field.

Funding information statement

Hereby, the authors declare that they did not receive any funding for this manuscript.

Conflict of interest statement

Hereby, the authors declare that they have no known competing financial interests or personal relationships that could have appeared to influence the work reported in this paper.

References

Abdulla, K. H., & Naser, H. A. (2021). Protection of marine environmental quality in the Kingdom of Bahrain. *Ocean and Coastal Management*, *203*(September 2020), 105520. https://doi.org/10.1016/j.ocecoaman.2021.105520

Abuhatab, S., El-Qanni, A., Al-Qalaq, H., Hmoudah, M., & Al-Zerei, W. (2020). Effective adsorptive removal of Zn2+, Cu2+, and Cr3+ heavy metals from aqueous solutions using silica-based embedded with NiO and MgO nanoparticles. *Journal of Environmental Management*, *268*(May), 110713. https://doi.org/10.1016/j.jenvman.2020.110713

Adam, A. M., Saad, H. A., Atta, A. A., Alsawat, M., Hegab, M. S., Altalhi, T. A., & Refat, M. S. (2021). *An Environmentally Friendly Method for Removing Hg(II), Pb(II), Cd(II) and Sn(II) Heavy Metals from Wastewater Using Novel Metal–Carbon-Based Composites Abdel*. *Ii*.

Aisida, S. O., Ahmad, I., & Ezema, F. I. (2020). Effect of calcination on the microstructural and magnetic properties of PVA, PVP and PEG assisted zinc ferrite nanoparticles. *Physica B: Condensed Matter*, *579*(October 2019), 411907. https://doi.org/10.1016/j.physb.2019.411907

Al-Najar, B., Khezami, L., Judith Vijaya, J., Lemine, O. M., & Bououdina, M. (2017). Effect of synthesis route on the uptake of Ni and Cd by MgFe2O4 nanopowders. *Applied Physics A: Materials Science and Processing*, *123*(1), 1–8. https://doi.org/10.1007/s00339-016-0710-7

Al Maashani, M. S., Khalaf, K. A., Gismelseed, A. M., & Al-Omari, I. A. (2020). The structural and magnetic properties of the nano-CoFe2O4 ferrite prepared by sol-gel auto-combustion technique. *Journal of Alloys and Compounds*, *817*, 152786. https://doi.org/10.1016/j.jallcom.2019.152786

Asadi, R., Abdollahi, H., Gharabaghi, M., & Boroumand, Z. (2020). Effective removal of Zn (II) ions from aqueous solution by the magnetic MnFe2O4 and CoFe2O4 spinel ferrite nanoparticles with focuses on synthesis, characterization, adsorption, and desorption. *Advanced Powder Technology*, *31*(4), 1480–1489. https://doi.org/10.1016/j.apt.2020.01.028

Ashok, A., Ratnaji, T., John Kennedy, L., & Judith Vijaya, J. (2020). Magnetically separable Zn1-xCuxFe2O4 ($0 \leq x \leq 0.5$) nanocatalysts for the transesterification of waste cooking oil. *Advanced Powder Technology*, *31*(6), 2573–2585. https://doi.org/https://doi.org/10.1016/j.apt.2020.04.022

Ashok, A., Ratnaji, T., John Kennedy, L., Judith Vijaya, J., & Gnana Pragash, R. (2021). Magnetically recoverable Mg substituted zinc ferrite nanocatalyst for biodiesel production: Process optimization, kinetic and thermodynamic analysis. *Renewable Energy*, *163*, 480–494. https://doi.org/10.1016/j.renene.2020.08.081

Bersuder, P., Smith, A. J., Hynes, C., Warford, L., Barber, J. L., Losada, S., Limpenny, C., Khamis, A. S., Abdulla, K. H., Le Quesne, W. J. F., & Lyons, B. P. (2020). Baseline survey of marine sediments collected from the Kingdom of Bahrain: PAHs, PCBs, organochlorine pesticides, perfluoroalkyl substances, dioxins, brominated flame retardants and metal contamination. *Marine Pollution Bulletin*, *161*(September), 111734. https://doi.org/10.1016/j.marpolbul.2020.111734

Bhushan Das, S., Kumar Singh, R., Kumar, V., Kumar, N., & Kumar, S. (2021). Tailoring the structural, optical and multiferroic properties of low temperature synthesized cobalt ferrite nanomaterials, by citrate precursor method. *Materials Today: Proceedings*, *xxxx*, 1–7. https://doi.org/10.1016/j.matpr.2021.04.001

Bououdina, M., Alwqyan, T. S., Khezami, L., Al-Najar, B., Shaikh, M. N., Gill, R., Modwi, A., Taha, K. K., & Lemine, O. M. (2019). Fabrication and characterization of nanostructured MgO·Fe2O3 composite by mechanical milling as efficient adsorbent of heavy metals. *Journal of Alloys and Compounds*, *772*, 1030–1039. https://doi.org/10.1016/j.jallcom.2018.09.010

Çelebi, H., Gök, G., & Gök, O. (2020). Adsorption capability of brewed tea waste in waters containing toxic lead(II), cadmium (II), nickel (II), and zinc(II) heavy metal ions. *Scientific Reports*, *10*(1), 1–12. https://doi.org/10.1038/s41598-020-74553-4

Chauhan, G., González-González, R. B., & Iqbal, H. M. N. (2022). Bioremediation and decontamination potentials of metallic nanoparticles loaded nanohybrid matrices – A review. *Environmental Research*, *204*(September 2021). https://doi.org/10.1016/j.envres.2021.112407

Darling, S. B. (2018). Perspective: Interfacial materials at the interface of energy and water. *Journal of Applied Physics*, *124*(3). https://doi.org/10.1063/1.5040110

Derakhshani, M., Taheri-Nassaj, E., Jazirehpour, M., & Masoudpanah, S. M. (2021). Structural, magnetic, and gigahertz-range electromagnetic wave absorption properties of bulk Ni–Zn ferrite. *Scientific Reports*, *11*(1), 1–13. https://doi.org/10.1038/s41598-021-88930-0

Fayazzadeh, S., Khodaei, M., Arani, M., Mahdavi, S. R., Nizamov, T., & Majouga, A. (2020). Magnetic Properties and Magnetic Hyperthermia of Cobalt Ferrite Nanoparticles Synthesized by Hydrothermal Method. *Journal of Superconductivity and Novel Magnetism*. https://doi.org/10.1007/s10948-020-05490-6

Hareendran, A., Dais, E., Shinoy, D., Srikripa, S., Shibu, G. M., & Kurian, M. (2022). Nitrogen- and sulfur-doped zinc ferrite nanoparticles as efficient heterogeneous catalysts in advanced oxidation processes. *Journal of Physics and Chemistry of Solids*, *161*(May 2021), 110398. https://doi.org/10.1016/j.jpcs.2021.110398

Heiba, Z. K., Ghannam, M. M., Sanad, M. M. S., Albassam, A. A., & Mohamed, M. B. (2020). Structural, optical, and dielectric properties of nano-ZnMn2−xVxO4. *Journal of Materials Science: Materials in Electronics*, *31*(11), 8946–8962. https://doi.org/10.1007/s10854-020-03429-0

Ivanets, A. I., Prozorovich, V. G., Roshchina, M. Y., Srivastava, V., & Sillanpää, M. (2019). Unusual behavior of MgFe2O4 during regeneration: Desorption versus specific adsorption. *Water Science and Technology*, *80*(4), 654–658. https://doi.org/10.2166/wst.2019.307

Ivanets, A. I., Srivastava, V., Roshchina, M. Y., Sillanpää, M., Prozorovich, V. G., & Pankov, V. V. (2018). Magnesium ferrite nanoparticles as a magnetic sorbent for the removal of Mn2+, Co2+, Ni2+ and Cu2+ from aqueous solution. *Ceramics International*, *44*(8), 9097–9104. https://doi.org/https://doi.org/10.1016/j.ceramint.2018.02.117

Ivanets, A., Prozorovich, V., Kouznetsova, T., Dontsova, T., Yanushevska, O., Hosseini-Bandegharaei, A., Srivastava, V., & Sillanpää, M. (2021a). Effect of Mg2+ ions on competitive metal ions adsorption/desorption on magnesium ferrite: Mechanism, reusability and stability studies. *Journal of Hazardous Materials*, *411*(December 2020), 1–9. https://doi.org/10.1016/j.jhazmat.2020.124902

Ivanets, A., Prozorovich, V., Kouznetsova, T., Dontsova, T., Yanushevska, O., Hosseini-Bandegharaei, A., Srivastava, V., & Sillanpää, M. (2021b). Effect of Mg2+ ions on competitive metal ions adsorption/desorption on magnesium ferrite: Mechanism, reusability and stability studies. *Journal of Hazardous Materials*, *411*(January), 1–9. https://doi.org/10.1016/j.jhazmat.2020.124902

Ivanets, A., Prozorovich, V., Roshchina, M., Kouznetsova, T., Budeiko, N., Kulbitskaya, L., Hosseini-Bandegharaei, A., Masindi, V., & Pankov, V. (2021a). A comparative study on the synthesis of magnesium ferrite for the adsorption of metal ions: Insights into the essential role of crystallite size and surface hydroxyl groups. *Chemical Engineering Journal*, *411*, 128523. https://doi.org/https://doi.org/10.1016/j.cej.2021.128523

Ivanets, A., Prozorovich, V., Roshchina, M., Kouznetsova, T., Budeiko, N., Kulbitskaya, L., Hosseini-Bandegharaei, A., Masindi, V., & Pankov, V. (2021b). A comparative study on the

synthesis of magnesium ferrite for the adsorption of metal ions: Insights into the essential role of crystallite size and surface hydroxyl groups. *Chemical Engineering Journal*, *411*(January), 128523. https://doi.org/10.1016/j.cej.2021.128523

Jasrotia, R., Singh, V. P., Kumar, R., & Singh, M. (2020). Raman spectra of sol-gel auto-combustion synthesized Mg-Ag-Mn and Ba-Nd-Cd-In ferrite based nanomaterials. *Ceramics International*, *46*(1), 618–621. https://doi.org/10.1016/j.ceramint.2019.09.012

Jyothish, B., & Jacob, J. (2021). Al-doped zinc ferrite nanoparticles: Preparation and evaluation of thermal, structural, morphological and anticancer properties. *Journal of Alloys and Compounds*, *863*. https://doi.org/10.1016/j.jallcom.2020.158352

Keerthana, S. P., Yuvakkumar, R., Ravi, G., Al-Sehemi, A. G., & Velauthapillai, D. (2022). Synthesis of pure and lanthanum-doped barium ferrite nanoparticles for efficient removal of toxic pollutants. *Journal of Hazardous Materials*, *424*(PC), 127604. https://doi.org/10.1016/j.jhazmat.2021.127604

Khizar, S., Ahmad, N. M., Ahmed, N., Manzoor, S., Hamayun, M. A., Naseer, N., Tenório, M. K. L., Lebaz, N., & Elaissari, A. (2020). Aminodextran coated CoFe2O4 nanoparticles for combined magnetic resonance imaging and hyperthermia. *Nanomaterials*, *10*(11), 1–16. https://doi.org/10.3390/nano10112182

Khoso, W. A., Haleem, N., Baig, M. A., & Jamal, Y. (2021). Synthesis, characterization and heavy metal removal efficiency of nickel ferrite nanoparticles (NFN's). *Scientific Reports*, *11*(1), 1–10. https://doi.org/10.1038/s41598-021-83363-1

Kinuthia, G. K., Ngure, V., Beti, D., Lugalia, R., Wangila, A., & Kamau, L. (2020). Levels of heavy metals in wastewater and soil samples from open drainage channels in Nairobi, Kenya: community health implication. *Scientific Reports*, *10*(1), 1–13. https://doi.org/10.1038/s41598-020-65359-5

Kmita, A., Żukrowski, J., Kuciakowski, J., Marciszko-Wiąckowska, M., Żywczak, A., Lachowicz, D., Gajewska, M., & Sikora, M. (2021). Effect of Thermal Treatment at Inert Atmosphere on Structural and Magnetic Properties of Non-stoichiometric Zinc Ferrite Nanoparticles. *Metallurgical and Materials Transactions A: Physical Metallurgy and Materials Science*, *52*(5), 1632–1648. https://doi.org/10.1007/s11661-021-06154-3

Król, A., Mizerna, K., & Bożym, M. (2020). An assessment of pH-dependent release and mobility of heavy metals from metallurgical slag. *Journal of Hazardous Materials*, *384*(July 2019). https://doi.org/10.1016/j.jhazmat.2019.121502

Liu, W., Zhou, Y., Bao, J., Wang, J., Zhang, Y., Sheng, X., Xue, Y., Guo, C., & Chen, X. (2020). Co-CoO/ZnFe2O4 encapsulated in carbon nanowires derived from MOFs as electrocatalysts for hydrogen evolution. *Journal of Colloid and Interface Science*, *561*, 620–628. https://doi.org/10.1016/j.jcis.2019.11.037

Long, W., Hamza, M. U., Abdul-Fattah, M. N., Rheima, A. M., Ahmed, Y. M., Fahim, F. S., Altimari, U. S., Aldulaim, A. K. O., Janani, B. J., & Fakhri, A. (2022). Preparation, photocatalytic and antibacterial studies on novel doped ferrite nanoparticles: Characterization and Mechanism evaluation. *Colloids and Surfaces A: Physicochemical and Engineering Aspects*, *650*(March), 129468. https://doi.org/10.1016/j.colsurfa.2022.129468

Ma, J., Wang, H., Zhang, M., Li, D., Liu, L., & Yang, H. (2020). Preparation of terpyridine-functionalized paramagnetic nickel-zinc ferrite microspheres for adsorbing Pb(II), Hg(II), and Cd(II) from water. *RSC Advances*, *10*(65), 39468–39477. https://doi.org/10.1039/d0ra06746f

Mariosi, F. R., Venturini, J., da Cas Viegas, A., & Bergmann, C. P. (2020). Lanthanum-doped spinel cobalt ferrite (CoFe2O4) nanoparticles for environmental applications. *Ceramics International*, *46*(3), 2772–2779. https://doi.org/10.1016/j.ceramint.2019.09.266

Mary, B. C. J., Vijaya, J. J., Bououdina, M., Kennedy, L. J., Khezami, L., & Modwi, A. (2023). Adsorption ability of aqueous lead (II) by NiFe2O4 and 2D- rGO decorated NiFe2O4 nanocomposite. In *Journal of Materials Science: Materials in Electronics* (Vol. 34, Issue 9). Springer US. https://doi.org/10.1007/s10854-023-10237-9

Miranda, L. S., Ayoko, G. A., Egodawatta, P., & Goonetilleke, A. (2022). Adsorption-desorption behavior of heavy metals in aquatic environments: Influence of sediment, water and metal ionic properties. *Journal of Hazardous Materials*, *421*(July 2021), 126743. https://doi.org/10.1016/j.jhazmat.2021.126743

Mmelesi, O. K., Masunga, N., Kuvarega, A., Nkambule, T. T., Mamba, B. B., & Kefeni, K. K. (2021). Cobalt ferrite nanoparticles and nanocomposites: Photocatalytic, antimicrobial activity and toxicity in water treatment. *Materials Science in Semiconductor Processing*, *123*(April 2020), 105523. https://doi.org/10.1016/j.mssp.2020.105523

Nasiri, R., Arsalani, N., & Panahian, Y. (2018). One-pot synthesis of novel magnetic three-dimensional graphene/chitosan/nickel ferrite nanocomposite for lead ions removal from aqueous solution: RSM modelling design. *Journal of Cleaner Production*, *201*, 507–515. https://doi.org/10.1016/j.jclepro.2018.08.059

Nimshi, R. E., Vijaya, J. J., Kennedy, L. J., Selvamani, P. S., Bououdina, M., & Sophia, P. J. (2023). Effective microwave assisted synthesis of CoFe2O4@TiO2@rGO ternary nanocomposites for the synergic sonophotocatalytic degradation of tetracycline and c antibiotics. *Ceramics International*, *49*(9, Part A), 13762–13773. https://doi.org/https://doi.org/10.1016/j.ceramint.2022.12.254

Obasi, P. N., & Akudinobi, B. B. (2020). Potential health risk and levels of heavy metals in water resources of lead–zinc mining communities of Abakaliki, southeast Nigeria. *Applied Water Science*, *10*(7), 1–23. https://doi.org/10.1007/s13201-020-01233-z

Ong, C. B., Ng, L. Y., & Mohammad, A. W. (2018). A review of ZnO nanoparticles as solar photocatalysts: Synthesis, mechanisms and applications. *Renewable and Sustainable Energy Reviews*, *81*(July 2016), 536–551. https://doi.org/10.1016/j.rser.2017.08.020

Paul, D. (2017). Research on heavy metal pollution of river Ganga: A review. *Annals of Agrarian Science*, *15*(2), 278–286. https://doi.org/10.1016/j.aasci.2017.04.001

Punia, P., Aggarwal, R. K., Kumar, R., Dhar, R., Thakur, P., & Thakur, A. (2022). Adsorption of Cd and Cr ions from industrial wastewater using Ca doped Ni–Zn nanoferrites: Synthesis, characterization and isotherm analysis. *Ceramics International*, *48*(13), 18048–18056. https://doi.org/10.1016/j.ceramint.2022.02.234

Rashdan, S. A., & Hazeem, L. J. (2020). Synthesis of spinel ferrites nanoparticles and investigating their effect on the growth of microalgae Picochlorum sp. *Arab Journal of Basic and Applied Sciences*, *27*(1), 134–141. https://doi.org/10.1080/25765299.2020.1733174

Rastgar, M., Shakeri, A., Bozorg, A., Salehi, H., & Saadattalab, V. (2017). Impact of nanoparticles surface characteristics on pore structure and performance of forward osmosis membranes. *Desalination*, *421*, 179–189. https://doi.org/10.1016/j.desal.2017.01.040

Reddy, D. H. K., & Yun, Y. S. (2016). Spinel ferrite magnetic adsorbents: Alternative future materials for water purification? *Coordination Chemistry Reviews*, *315*, 90–111. https://doi.org/10.1016/j.ccr.2016.01.012

Rivero, M., Del Campo, A., Mayoral, Á., Mazario, E., Sánchez-Marcos, J., & Muñoz-Bonilla, A. (2016). Synthesis and structural characterization of ZnxFe3-xO4 ferrite nanoparticles obtained by an electrochemical method. *RSC Advances*, *6*(46), 40067–40076. https://doi.org/10.1039/c6ra04145k

Sahoo, T. R., & Prelot, B. (2020). Adsorption processes for the removal of contaminants from wastewater: The perspective role of nanomaterials and nanotechnology. In *Nanomaterials for the Detection and Removal of Wastewater Pollutants*. Elsevier Inc. https://doi.org/10.1016/B978-0-12-818489-9.00007-4

Shah, J., Jain, S., Gahtori, B., Sharma, C., & Kotnala, R. K. (2021). Water splitting on the mesoporous surface and oxygen vacancies of iron oxide generates electricity by hydroelectric cell. *Materials Chemistry and Physics*, *258*(October 2020), 123981. https://doi.org/10.1016/j.matchemphys.2020.123981

Shakil, M., Inayat, U., Khalid, N. R., Tanveer, M., Gillani, S. S. A., Tariq, N. H., Shah, A., Mahmood, A., & Dahshan, A. (2022). Enhanced structural, optical, and photocatalytic activities of Cd–Co doped Zn ferrites for degrading methyl orange dye under irradiation by visible light. *Journal of Physics and Chemistry of Solids*, *161*(November 2020), 110419. https://doi.org/10.1016/j.jpcs.2021.110419

Shan, R., Shi, Y., Gu, J., Wang, Y., & Yuan, H. (2020). Single and competitive adsorption affinity of heavy metals toward peanut shell-derived biochar and its mechanisms in aqueous systems. *Chinese Journal of Chemical Engineering*, *28*(5), 1375–1383. https://doi.org/10.1016/j.cjche.2020.02.012

Shanmugavani, A., & Selvan, R. K. (2014). Synthesis of ZnFe2O4 nanoparticles and their asymmetric configuration with Ni(OH)2 for a pseudocapacitor. *RSC Advances*, *4*(51), 27022–27029. https://doi.org/10.1039/c4ra01793e

Slatineanu, T., Iordan, A. R., Palamaru, M. N., Caltun, O. F., Gafton, V., & Leontie, L. (2011). Synthesis and characterization of nanocrystalline Zn ferrites substituted with Ni. *Materials Research Bulletin*, *46*(9), 1455–1460. https://doi.org/10.1016/j.materresbull.2011.05.002

Somvanshi, S. B., Khedkar, M. V., Kharat, P. B., & Jadhav, K. M. (2020). Influential diamagnetic magnesium (Mg2+) ion substitution in nano-spinel zinc ferrite (ZnFe2O4): Thermal, structural, spectral, optical and physisorption analysis. *Ceramics International*, *46*(7), 8640–8650. https://doi.org/10.1016/j.ceramint.2019.12.097

Soultanidis, V., Papaspyros, I., Voudrias, E. A., & Moutsopoulos, K. N. (2022). Release of heavy metals from conventional and reflective cool cement pavements. *Journal of Cleaner Production*, *336*(December 2021), 130434. https://doi.org/10.1016/j.jclepro.2022.130434

Tang, J., Wu, W., Yu, L., Fan, X., Liu, G., & Yu, Y. (2019). Study on adsorption properties and mechanism of thallium onto titanium-iron magnetic adsorbent. *Science of the Total Environment*, *694*, 133625. https://doi.org/10.1016/j.scitotenv.2019.133625

Tatarchuk, T., Myslin, M., Lapchuk, I., Shyichuk, A., Murthy, A. P., Gargula, R., Kurzydło, P., Bogacz, B. F., & Pędziwiatr, A. T. (2021). Magnesium-zinc ferrites as magnetic adsorbents for Cr(VI) and Ni(II) ions removal: Cation distribution and antistructure modeling. *Chemosphere*, *270*. https://doi.org/10.1016/j.chemosphere.2020.129414

Tatarchuk, T., Naushad, M., Tomaszewska, J., Kosobucki, P., Myslin, M., Vasylyeva, H., & Ścigalski, P. (2020). Adsorption of Sr(II) ions and salicylic acid onto magnetic magnesium-zinc ferrites: isotherms and kinetic studies. *Environmental Science and Pollution Research*, *27*(21), 26681–26693. https://doi.org/10.1007/s11356-020-09043-1

Tatarchuk, T., Shyichuk, A., Sojka, Z., Gryboś, J., Naushad, M., Kotsyubynsky, V., Kowalska, M., Kwiatkowska-Marks, S., & Danyliuk, N. (2021). Green synthesis, structure, cations distribution and bonding characteristics of superparamagnetic cobalt-zinc ferrites nanoparticles for Pb(II) adsorption and magnetic hyperthermia applications. *Journal of Molecular Liquids*, *328*. https://doi.org/10.1016/j.molliq.2021.115375

Tengvall, P. (2011). 4.406 - Protein Interactions with Biomaterials. In P. Ducheyne (Ed.),

Comprehensive Biomaterials (pp. 63–73). Elsevier. https://doi.org/https://doi.org/10.1016/B978-0-08-055294-1.00006-4

Tho, P. T., Van, H. T., Nguyen, L. H., Hoang, T. K., Ha Tran, T. N., Nguyen, T. T., Hanh Nguyen, T. B., Nguyen, V. Q., Le Sy, H., Thai, V. N., Tran, Q. B., Sadeghzadeh, S. M., Asadpour, R., & Thang, P. Q. (2021). Enhanced simultaneous adsorption of As(iii), Cd(ii), Pb(ii) and Cr(vi) ions from aqueous solution using cassava root husk-derived biochar loaded with ZnO nanoparticles. *RSC Advances*, *11*(31), 18881–18897. https://doi.org/10.1039/d1ra01599k

Thomas, B., & Alexander, L. K. (2020). Removal of Pb2+ and Cd2+ toxic heavy metal ions driven by Fermi level modification in NiFe2O4–Pd nano hybrids. *Journal of Solid State Chemistry*, *288*(April), 121417. https://doi.org/10.1016/j.jssc.2020.121417

Thota, S., Kashyap, S. C., Sharma, S. K., & Reddy, V. R. (2016). Micro Raman, Mossbauer and magnetic studies of manganese substituted zinc ferrite nanoparticles: Role of Mn. *Journal of Physics and Chemistry of Solids*, *91*, 136–144. https://doi.org/10.1016/j.jpcs.2015.12.013

Toby, B. H. (2006). R factors in Rietveld analysis: How good is good enough? . *Powder Diffraction*, *21*(1), 67–70. https://doi.org/10.1154/1.2179804

Tran, C. Van, Quang, D. V., Nguyen Thi, H. P., Truong, T. N., & La, D. D. (2020). Effective Removal of Pb(II) from Aqueous Media by a New Design of Cu-Mg Binary Ferrite. *ACS Omega*, *5*(13), 7298–7306. https://doi.org/10.1021/acsomega.9b04126

Vinosha, P. A., Mely, L. A., Jeronsia, J. E., Krishnan, S., & Das, S. J. (2017). Synthesis and properties of spinel ZnFe2O4 nanoparticles by facile co-precipitation route. *Optik*, *134*, 99–108. https://doi.org/10.1016/j.ijleo.2017.01.018

Vinosha, P. A., Vinsla, J. V. A., Madhavan, J., Devanesan, S., AlSalhi, M. S., Nicoletti, M., & Xavier, B. (2022a). Impact of dysprosium doped (Dy) zinc ferrite (ZnFe2o4) nanocrystals in photo-fenton exclusion of recalcitrant organic pollutant. *Environmental Research*, *203*(July 2021), 111913. https://doi.org/10.1016/j.envres.2021.111913

Vinosha, P. A., Vinsla, J. V. A., Madhavan, J., Devanesan, S., AlSalhi, M. S., Nicoletti, M., & Xavier, B. (2022b). Impact of dysprosium doped (Dy) zinc ferrite (ZnFe2o4) nanocrystals in photo-fenton exclusion of recalcitrant organic pollutant. *Environmental Research*, *203*. https://doi.org/10.1016/j.envres.2021.111913

Wang, F., Chen, D., Zhang, N., Wang, S., Qin, L., Sun, X., & Huang, Y. (2017). Oxygen vacancies induced by zirconium doping in bismuth ferrite nanoparticles for enhanced photocatalytic performance. *Journal of Colloid and Interface Science*, *508*, 237–247. https://doi.org/https://doi.org/10.1016/j.jcis.2017.08.056

Wang, J., & Guo, X. (2020). Adsorption isotherm models: Classification, physical meaning, application and solving method. *Chemosphere*, *258*, 127279. https://doi.org/10.1016/j.chemosphere.2020.127279

Wang, M., Cheng, L., Huang, L., Pan, S., Yao, Q., Hu, C., Liang, Q., & Zhou, H. (2021). Effect of Sr doped the YFeO3 rare earth ortho-ferrite on structure, magnetic properties, and microwave absorption performance. *Ceramics International*, *47*(24), 34159–34169. https://doi.org/10.1016/j.ceramint.2021.08.325

Wu, C., Tu, J., Tian, C., Geng, J., Lin, Z., & Dang, Z. (2018). Defective magnesium ferrite nano-platelets for the adsorption of As(V): The role of surface hydroxyl groups. *Environmental Pollution*, *235*, 11–19. https://doi.org/10.1016/j.envpol.2017.12.050

Wu, C., Xu, Y., Xu, S., Tu, J., Tian, C., & Lin, Z. (2019). Enhanced adsorption of arsenate by spinel zinc ferrite nano particles: Effect of zinc content and site occupation. *Journal of Environmental Sciences (China)*, *79*, 248–255. https://doi.org/10.1016/j.jes.2018.09.010

Xiang, Y., Yang, X., Xu, Z., Hu, W., Zhou, Y., Wan, Z., Yang, Y., Wei, Y., Yang, J., & Tsang, D. C. W. (2020). Fabrication of sustainable manganese ferrite modified biochar from vinasse for enhanced adsorption of fluoroquinolone antibiotics: Effects and mechanisms. *Science of the Total Environment*, *709*, 136079. https://doi.org/10.1016/j.scitotenv.2019.136079

Yang, W., Wang, Z., Song, S., Han, J., Chen, H., Wang, X., Sun, R., & Cheng, J. (2019). Adsorption of copper(II) and lead(II) from seawater using hydrothermal biochar derived from Enteromorpha. *Marine Pollution Bulletin*, *149*(September), 110586. https://doi.org/10.1016/j.marpolbul.2019.110586

Zakiyah, L. B., Saion, E., Al-Hada, N. M., Gharibshahi, E., Salem, A., Soltani, N., & Gene, S. (2015). Up-scalable synthesis of size-controlled copper ferrite nanocrystals by thermal treatment method. *Materials Science in Semiconductor Processing*, *40*, 564–569. https://doi.org/10.1016/j.mssp.2015.07.027

Zhang, H., Li, H., Gao, D., & Yu, H. (2022). Source identification of surface water pollution using multivariate statistics combined with physicochemical and socioeconomic parameters. *Science of the Total Environment*, *806*, 151274. https://doi.org/10.1016/j.scitotenv.2021.151274

Zhao, W., Chen, I. W., & Huang, F. (2019). Toward large-scale water treatment using nanomaterials. *Nano Today*, *27*, 11–27. https://doi.org/10.1016/j.nantod.2019.05.003